UNIVERSITY OF BAYREUTH – MICROMETEOROLOGY

Bachelor Thesis

Characterizing summer nighttime urban heat island intensity and cold-air dynamics through mobile flux measurements and stationary sensor networks in a mid-sized city in central Europe

Sophie Resch

September 2025

Supervised by

Prof. Dr. Christoph Thomas

Dr. Wolfgang Babel

Abstract

Ongoing urbanization and climate change are intensifying health risks from urban heat stress, particularly during nighttime. Therefore, a fundamental understanding of the processes that shape the urban boundary layer climate is becoming increasingly important. This thesis investigates nocturnal urban heat island (UHI) intensity and the role of cold-air dynamics in mitigating nighttime heat retention. To quantify the magnitude of thermal contrasts and investigate the role of land use in shaping nocturnal microclimates, a combination of stationary and bike-based mobile measurements was conducted at street-canyon scale during the summer of 2024 in the city district St. Georgen/Burg of Bayreuth, Germany. Additional to temperature and humidity coverage with the mobile set up, an approach was made to measure turbulent fluxes by using a mobile Eddy Covariance (EC) system on the cargo bike for the characterization of turbulent exchange processes. To ensure nearly steady-state conditions, the perturbation and averaging periods were fitted to calculate flux densities along approximately homogeneous street transects.

The results reveal pronounced spatial and temporal heterogeneity in nocturnal thermal conditions, with UHI intensities reaching up to 5 K. Positive heat fluxes indicate ongoing heat release from urban surfaces and anthropogenic sources. Despite the short EC averaging periods, the mobile flux measurements successfully captured differences in flux densities across heterogeneous urban environments. The spatial temperature patterns highlight clear differences between urban and semi-urban locations, implying that the district has a lack of effective cold-air ventilation pathways, with spatial temperature differences increasing under radiative cooling conditions.

This thesis demonstrates the complex interplay between land use, urban form and atmospheric dynamics in shaping nighttime urban climates. The combined measurements provide a foundation for science-based heat adaptation strategies, supporting urban planning efforts to reduce UHI effects and related health risks.

Contents

List of abbreviations

Abbreviation	Description
UHI	Urban Heat Island
MWS	Micro weather stations
EC	Eddy Covariance
EBG	Ecological botanical garden
LS	Leersstraße
RH	Retirement home
CF	Correction facility
AA	Allotment association
TP	Tekirdagplatz
GY	Graveyard
WA	Wilhelminenaue
SG	St. Georgen Street

List of figures

List of tables

1. Introduction

1.1 Motivation

Against the backdrop of increasingly noticeable impacts of climate change, the need for adaptation to rising temperatures and more frequent and severe heat waves has become more urgent. The most recent report of the Intergovernmental Panel on Climate Change demonstrates that global warming is not only continuing but is already causing significant shifts in climate and weather extremes in many regions (IPCC, 2023).

These developments coincide with demographic change. The proportion of older individuals is steadily growing in the western civilisation. Older people as well as young children are mostly affected by heat stress and suffer from extreme temperatures so that these climate change dynamics lead to increased health risks (Klein Rosenthal et al., 2014). Additionally, due to the ongoing trend of urbanization, it is expected that around 66% of the world's population will live in urban areas by 2050 (United Nations Department of Economic and Social Affairs, 2014). This trend shifts the focus towards urban climate phenomena like the Urban Heat Island (UHI) Effect. The effect describes the temperature difference between urban areas and their rural surroundings. Densely built areas with less vegetation and more concrete lead to higher temperatures, especially during nights (Oke, 1987).

With its geographical location in Central Europe, Germany lies in a transitional zone between the maritime Atlantic climate and the dry continental climate. This positioning exposes the region to both humid westerly and dry easterly air masses, making it particularly sensitive to climate variability. Bavaria, in particular, experiences stronger impacts of climate change compared to many other regions in Germany. Due to a distance from moderating oceanic influences and the orographic effects of both the low mountain ranges and the Alps, climatic extremes such as heat waves, droughts, and intense precipitation events are amplified (Foken, 2007). The number of hot days averaged across Germany has almost quadrupled since the 1950s (Deutscher Wetterdienst, 2024). The rate of warming in Upper

Franconia – the region around Bayreuth – is approximately 2.5 times higher than the global average (Thomas, 2025).

While the UHI in Bayreuth has already been investigated in several projects at different sites, this study specifically focuses on the St. Georgen/Burg district in the northern part of the city (e.g. Foken, 2007; Schappacher, 2024; Spies, 2019; Tschuschke, 2019). In view of the increasing heat stress due to climate change, cold-air flows have been a subject of research in Bayreuth for several years. In this context, efforts are being made to preserve and maintain cold-air corridors that facilitate the inflow of cooler air masses into the urban area.

In addition to existing initiatives, the municipality of Bayreuth has started a new project on developing heat adaption strategies (Stadt Bayreuth, 2025). The work presented in this thesis is included to support considerations and decisions regarding urban development measures. Particular attention is paid to nocturnal heat stress, which poses significant health risks (Beckmann et al., 2021). The role of cold-air inflow, the spatial distribution of air temperature during the night and the early morning transition were investigated in this context.

This thesis takes a novel approach by conducting mobile measurement campaigns to determine flux densities, thereby providing high resolution data of momentum and turbulent energy fluxes. For this purpose, an Eddy Covariance (EC) measurement device was mounted on a mobile platform on a cargo bike, allowing flux measurements to be conducted along different transects within the St. Georgen/Burg district. This approach enables a spatially explicit characterization of turbulent exchange processes in the urban environment.

1.2 Theoretical background

This chapter covers the theoretical foundations of the thesis, focusing on the UHI effect and cold air build up, flow and accumulation. Additionally, it provides a brief introduction to EC.

1.2.1 Urban Heat Island Effect

Especially during the night, it can be observed that urban areas have higher temperatures than their rural surroundings. The term Urban Heat Island (UHI) has been established for this phenomenon, as cities are like warm landmass in a sea of cooler rural surrounding (Oke, 1969). The intensity of the UHI is generally defined as the temperature difference ΔT_{UHI} between the urban and the rural area with the urban temperature T_{urban} and the rural temperature T_{rural} (1.1).

$$\Delta T_{UHI} = T_{urban} - T_{rural} \tag{1.1}$$

The UHI definition is formulated in a general way to pursue the idea that multiple types of UHIs exist, depending on specific characteristics and driven by different energy exchange processes. The intensity of the UHI is known to increase under conditions of low wind speed, reduced cloud cover, anticyclonic weather situations, during summer and during nights (Arnfield, 2003). Moreover, it depends on the urban form, particularly the building density, as well as on the size of the city and, consequently, its population (Oke, 1973).

The UHI develops from changes of the surface and atmosphere resulting in a change in energy balance (Oke et al., 2017). During the day, incoming radiation is absorbed and stored as energy by typical urban materials such as asphalt and stone due to their low albedo and high heat capacity. At night, the stored energy is emitted as longwave radiation, which is partly trapped in dense street canyons, contributing to elevated nighttime temperatures. Furthermore, reduced vegetation cover leads to less cooling through evapotranspiration, while additional anthropogenic heat sources increase the urban temperatures. At night, the main differences between rural and urban areas are driven by the significantly higher storage change term ΔQ_S, reflecting the release of the energy stored during the day as well as the persistence of anthropogenic heat emissions.

This relationship can be expressed by the surface energy balance:

$$-Q^* = Q_H + Q_E + Q_G + Q_{anthr} + \Delta Q_S \tag{1.2}$$

(after Arnfield, 2003)

Q^*: net radiative flux (longwave + shortwave)

Q_H: sensible heat flux

Q_E: latent heat flux

Q_G: ground heat flux

Q_{anthr}: anthropogenic heat flux

ΔQ_S: Storage change term

The altered energy fluxes cause changes to the planetary boundary layer (PBL). This effect is particularly pronounced in conditions with low wind speeds and high levels of radiation. Depending on the layout of the buildings, the PBL is divided into the urban mixing layer (UML), the surface layer (SL), the urban roughness sublayer (RSL) and urban canopy layer (UCL) (Kuttler & Weber, 2023).

SL and UML together form the UBL (urban boundary layer), which is characteristic of a city. The UML continues above the RBL (rural boundary layer) downwind as an urban plume and can reattach to the ground again far away from the city under the right flow conditions, which is why urban climatic conditions can also develop outside the city. The UBL and RBL are caused by the roughness jumps before and after the built-up area of the city (Kuttler & Weber, 2023).

The research takes place in the UCL of Bayreuth, constituting the lowest part of the RSL, extending from the ground surface up to the mean building height. Due to the limited convective and radiative coupling between the air volume within the canopy and the RSL above roof level, the UCL is able to maintain its own distinct microclimate. However, these microclimatic effects are spatially constrained, dissipating over relatively short distances through horizontal and vertical turbulent mixing (Feigenwinter et al., 2012).

1.2.2 Cold air flow and accumulation

Cold air formation typically occurs under anticyclonic weather conditions during calm and clear nights. The cloudlessness combined with low wind speeds enhances the radiative cooling. Since shortwave radiation is negligible (S↓, S↑) during night, and the clear sky conditions result in minimal atmospheric downward longwave radiation (L↓), the long-wave radiation balance is positive (L↑ > L↓). This leads to a net energy loss at the Earth's surface, which causes it to cool down (Häckel, 2021; Thomas & Babel, 2022). The low wind speeds provide no effective mixing of cooled air. Therefore, the limited mixing prevents the turbulent transport of warm air down to the cool surface. The radiation balance of the surface can be expressed as shown in (1.3).

$$S \downarrow + S \uparrow + L \downarrow + L \uparrow = -Q^* \quad (1.3)$$

S ↓: downward shortwave radiation

S ↑: reflected upward shortwave radiation

L ↓: downward longwave radiation (emitted by atmosphere)

L ↑: upward longwave radiation (emitted by earth surface)

Q∗: net radiation

As a result of radiative surface cooling, a thin layer of cold air develops on the ground. Due to its higher density compared to the surrounding warmer air, the cold air accumulates close to the surface. On sloped terrain, this density difference drives a gravity-induced, terrain-following downslope movement, commonly referred to as a katabatic flow or cold-air drainage (Häckel, 2021; Haiden & Whiteman, 2005; Thomas & Babel, 2022, 2023).

Cold-air flows play an essential role in urban cooling, as they help mitigating the intensity of the night UHI. By lowering nocturnal air temperatures, they ensure that the morning warming starts from a cooler baseline dampening the daytime temperature maxima. Since urban development and dense building structures can block or weaken these flows, it is essential to integrate cold-air corridors into urban planning strategies to maintaining their cooling function (Foken, 2007).

1.2.3 Eddy Covariance

The Eddy Covariance (EC) method is a micrometeorological approach used to quantify the exchange of heat, mass, and momentum between a flat, horizontally homogeneous surface and the overlying atmosphere. Under such conditions, the net transport between the surface and the atmosphere can be considered one-dimensional, so that vertical flux densities can be derived from the covariance between turbulent fluctuations of the vertical wind component and the respective variable quantity of interest (Aubinet et al., 2012).

The calculation of these fluxes requires several assumptions (Aubinet et al., 2012; Foken & Mauder, 2024b):

- Steady state conditions and horizontal homogeneity are assumed in the atmospheric boundary layer.
- Time series and values are decomposed using the Reynolds decomposition into mean and fluctuating components.
- Raw density or molar concentrations from the gas analyser are converted into pressure invariant mixing ratios (mass or molar) to correct for artifacts due to temperature, pressure, and water vapor fluctuations (WPL corrections).
- Density fluctuations are neglected except in the buoyancy term (Boussinesq approximation).

Under these assumptions, the vertical flux F (heat, water vapor, CO_2, etc.) is calculated as the mean of the product of the vertical wind fluctuation (w′) and the fluctuation of the scalar (x′) over a given timeframe:

$$\overline{w'x'} = \frac{1}{N-1}\sum_{k=0}^{N-1}\left[(w_k - \overline{w_k})(x_k - \overline{x_k})\right] = \\ = \frac{1}{N-1}\left[\sum_{k=0}^{N-1} w_k \cdot x_k - \frac{1}{N}\left(\sum_{k=0}^{N-1} w_k \sum_{k=0}^{N-1} x_k\right)\right] \tag{1.4}$$

(Foken & Mauder, 2024)

Here the fluctuations are expressed as deviations from the mean of that timeframe: $w' = w_k - \overline{w_k}$ and $x' = x_k - \overline{x_k}$.

1.3 Objective and research questions

The objective of this thesis is to quantify and explain air temperature perturbation during the night and to quantify the influence of cold air dynamics on the research site St. Georgen/Burg district in the city of Bayreuth. Meteorological measures were made to detect the underlying processes, with the focus on air temperature, vapor pressure and flux densities. The meteorological conditions in the research area were determined at two different spatial scales: a network of micro weather stations distributed throughout St. Georgen/Burg and mobile measurements in the street canyon were used. This database was used to investigate the following research questions which led, in combination with the priorly presented current state of knowledge, to the research questions and hypotheses:

RQ1: How does the UHI effect manifest spatially and temporally in Bayreuth during summer nights, and how do different locations and synoptic conditions influence nighttime heat retention, morning warming rates, tropical and cold air nights?

H1a: The intensity of the UHI effect is greater in areas with more building density and less vegetation, particularly under calm, clear weather conditions. This effect is most pronounced during cold air nights that are preceded by days with autochthonous conditions, as limited atmospheric mixing allows urban surfaces to retain more heat overnight.

H1b: Morning warming rates differ depending on land use, with distinct patterns observed across urban, semi-urban, and rural environments. Immediately after sunrise, rural areas warm up more rapidly than urban areas due to reduced shading and more open spaces, which allow for quicker solar induced heating.

RQ2: How frequently do radiation-induced cold-air nights occur in Bayreuth during summer, and how can cold-air drainage and accumulation be identified? How do topography and meteorological conditions influence these processes? How are sensible and latent heat flux densities distributed in the St. Georgen/Burg neighbourhood during cold air nights?

H2a: During radiation-induced cold-air nights, temperatures in rural areas are lower than in urban zones, with near-saturation relative humidity expected in these rural sites due to cold air pooling. Furthermore, cold-air drainage patterns closely follow the local topography, resulting in directional flow along valleys and accumulation in depressions.

H2b: Sensible heat fluxes are higher and generally positive in urban areas due to anthropogenic heat release, whereas in rural areas, especially where cold air accumulates, sensible heat fluxes approach zero or become slightly negative at night. Latent heat fluxes in rural areas are expected to be negative during these nights, reflecting condensation processes.

2. Methods

The measurements for this thesis were performed in the urban district of St. Georgen/Burg, as a part of the city of Bayreuth, Germany (49,95° N, 11,58° E) (Figure 2.1). Bayreuth is a medium-sized city with approximately 73,000 inhabitants and a total area of 67 km² (Bayerisches Landesamt für Statistik, 2024). The city is situated in a wide valley, surrounded by several hills, with an elevation range of about 100 m. The St. Georgen/Burg district in the northern part of Bayreuth is slightly elevated compared to the rest of the city. It compromises an industrial area, extensive residential areas, greener sections with vegetation around the school and the graveyard, as well as agricultural land adjacent to the correction facility. The district's main street is paved with dark cobblestones, while many of the older buildings are constructed from sandstone (Figure 2.5).

As rural reference, the meteorological station in the Ecological Botanical Garden (EBG) of the University of Bayreuth was used. Although located within the municipal boundaries of Bayreuth, the garden's temperature measurements are unaffected by urban structures. At the EBG Station the air temperature is measured in 2m height with a Frankenberger Psychrometer.

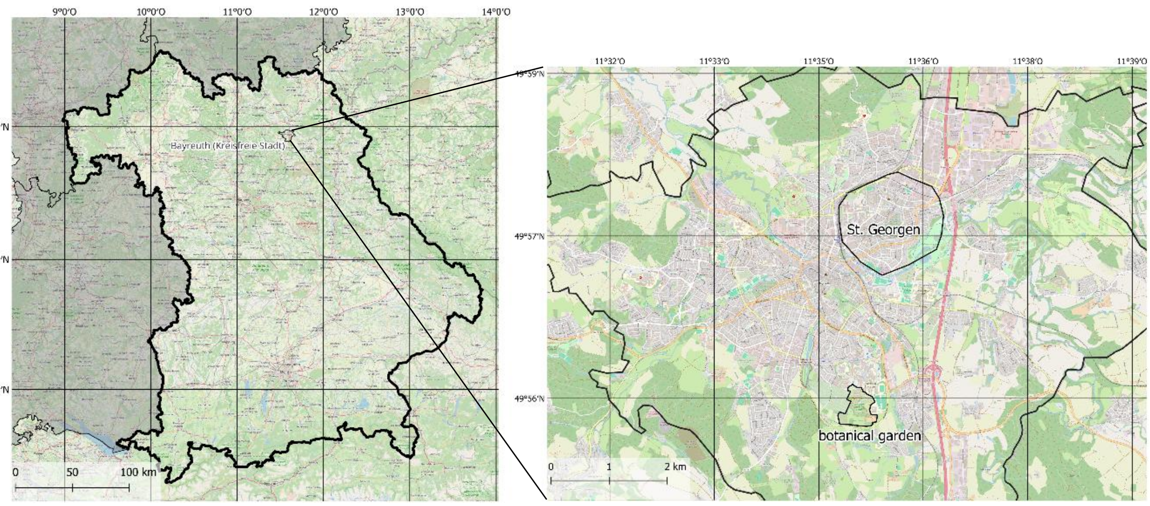

Figure 2.1 Left: Map of Bavaria (Germany), with investigation site Bayreuth. Right: City of Bayreuth with main area of investigation St. Georgen neighbourhood and the rural reference botanical garden. OpenStreetMap®, KBS = WGS 84

The time period of our measurements covers July and August 2024, aiming to capture the maximum potential heat stress for the residents. As this period typically represents the warmest part of the year in Bavaria and thus allows for a comprehensive assessment of extreme thermal conditions. Continuous measurements were taken from July 3rd until August 31st. The two-month timeframe provides a sufficient data base to identify both persistent patterns and short-term weather-related variations.

In this study two complementary measurement approaches were applied at different spatial scales to capture relevant weather elements. First, eight fully automated long-term micro weather stations (MWS) were installed on street lanterns and operated continuously throughout the entire measurement period. Second, these stationary observations were supplemented by mobile measurements on selected days using a cargo bike equipped with meteorological instruments at a measurement height of 1.60 m, enabling spatially continuous data collection.

2.1 Stationary measurements with MWS

For continuous measurements we used eight micro weather stations. Two stations were already set up at St. Georgen and at Wilhelminenaue during the MiSKOR Project (Minderung städtischer Klima- und Ozonrisiken, 01.04.2018 - 31.12.2020). The aim of this project was to quantify the urban climate and ozone pollution risks, in particular, to the inner-city distribution in order to reduce the negative consequences of the UHI effect and thus reduce the health risks for residents (Thomas et al., 2021). Since 2021, the micro weather stations have been operated by the Chair of Micrometeorology at the University of Bayreuth. The MWS (ATMOS41) with data logger (EM60G) were installed at street lanterns at a height of 3.5m (METER, 2019). An unused MiSKOR Station was moved to a meadow next to the St. Georgen graveyard, on a 2.5m pole. All MiSKOR data is logged to the bayEOS server of the University of Bayreuth. The remaining six stations (ATMOS41) with data logger (EM60G) were additionally set up at selected street lanterns in the St. Georgen neighborhood at a height of 3.5m. The data is logged to ZentraCloud (METER, 2019). All stations log the data with a five-minute time resolution as aggregation interval. The gust speed equates to the highest measured wind speed during the five-minute interval.

The parameters measured by the ATMOS41 stations can be found in Table 2.1.

Table 2.1 by ATMOS41 station measured parameters with symbols, units, resolution and accuracy. Internal fitted on the aggregation interval (METER, 2019).

Parameters	**Symbol**	**Unit**	**Resolution**	**Accuracy**
Air temperature	T	°C	0.1 °C	±0.6 °C
Solar radiation	$S\downarrow$	Wm^{-2}	1 Wm^{-2}	±5%
Wind direction	φ	°	1 °	±5°
Wind speed	u	ms^{-1}	0.01 ms^{-1}	±0.3 ms^{-1} or 3%
Gust speed	u_G	ms^{-1}	0.01 ms^{-1}	±0.3 ms^{-1} or 3%
Relative humidity	rH	%	0.1%	±3%
Vapor pressure	e	kPa	0.01 kPa	±0.2 kPa
Barometric pressure	p	kPa/hPa	0.01 kPa	±0.1 kPa

For this thesis the following meteorological variables were analyzed: air temperature, wind direction and speed, gust speed, vapor pressure and barometric pressure. Depending on the station configuration, either relative humidity or vapor pressure is recorded. In cases where only one was available, the other quantity was calculated using equation (2.1).

$$e = e_s \cdot \frac{rH}{100\ \%} \tag{2.1}$$

For this equation saturation vapor pressure e_s is needed and calculated with the Magnus formula (2.2). With the vapor pressure and the barometric pressure, the specific humidity q can be calculated (2.3).

$$e_s = 0.6112kPa \cdot \exp\left(\frac{17.62 \cdot T}{243.12°C + T}\right) \tag{2.2}$$

$$q = 0.622 \cdot \frac{e}{p - 0.32 \cdot e} \tag{2.3}$$

After a testing phase, the MWS were set up with the attempt to cover as much urban heterogeneity as possible. It should be noted that the station at Tekirdagplatz was only set up during August. Accordingly, in all subsequent plots covering the entire measurement period, TP represents data from August only. The locations of the MWS are shown in the following table (Table 2.2) and in Figure 2.5.

Table 2.2 Locations of Micro Weather Station with description of the research site, the locations are also presented in Figure 2.5.

Station	Coordinates	Description
Leersstraße (LS)	49.95628 N, 11.59522 E	residential area with detached apartment buildings
Retirement home (RH)	49.958430 N, 11.591167 E	next to a construction site, adjacent to a lower major road
Correction facility (CF)	49.95541 N, 11.58550 E	Between west entrance of the JVA site and agricultural ground
Allotment association (AA)	49.95573 N, 11.58280 E	at the bicycle lane crossing the allotment association gardens
Tekirdagplatz (TP)	49.951298 N, 11.587181 E	Square next to Brandenburger Straße with trees (only August)
Graveyard (GY)	49.95153 N, 11.59290 E	Tripod at a meadow south of the graveyard, next to bike lane
Wilhelminenaue (WA)	49.946492 N, 11.597678 E	Bikeway in the floodplain, next to the dam
St. Georgen main street (SG)	49.953974 N, 11.592077 E	In the middle of the densely built main street, without trees
Botanical Garden (EBG)	49.9247222 N, 11.586389 E	Measurement tower on a meadow, surrounded by trees, close to a pond

To ensure the proper functioning of the newly installed stations and to detect possible biases, the stations were placed next to the measurement tower at the Botanical Garden for approximately one week (21-26 June 2024). This set up enabled a comparison of the measured temperature and humidity to the reference data from the EBG tower. The comparison showed a significant bias in humidity at the GY station. The corresponding comparison plots are provided in the appendix (Figure A.1, Figure A. 2).

Since it was not fully possible to ensure the quality of the already set up stations a temperature error caused by a malfunction of the radiation sensor at the Wilhelminenaue station was later identified during the mobile measurement campaign. While this issue did not affect the nighttime measurements, the EBG station was subsequently selected as the rural reference in order to maintain comparability with the daytime study of Spakowski (2025). Also, all three MiSKOR stations (SG, WA, GY) will be excluded for any humidity and vapor pressure analysis, due to identified biases from unknown errors compared to the mobile measurements. The corresponding comparison plots are provided in the appendix (Figure A.3, Figure A.4).

2.1.1 Night classifications

To classify the analysed nights for further detailed investigation of synoptic situations, into cold-air nights, tropical nights, UHI nights or none of them, specific thresholds and criteria were applied for each category.

For the identification of cold-air nights, the criteria established by Schappacher (2024) were applied and adapted. The analysis is based on air temperature gradients between a cold-air-influenced and a non-influenced MWS in the Bayreuth city area, supplemented by gust speed, to ensure low wind conditions. The MWS Kämmerei, located in the city centre is not affected by cold-air flows, while the MWS Mistel, situated next to the river Mistel, in a cold air drainage path, is influenced by them. The distance between both stations is approximately 1 km. The applied thresholds are a minimum air temperature difference of 2.0 K and a maximum gust speed of 2.2 ms^{-1} at the Mistel station. To ensure the focus on nocturnal cold-air formation, the time period between 18:00 and 06:00 CEST was chosen.

To complement and refine this classification, measurements of net longwave radiation at the EBG station were added as a criterion. Since cold air builds up when there are mostly outgoing upward longwave radiation and no radiation remission from clouds, a high positive longwave radiation is expected. By combining both criteria in a joint analysis, the threshold for longwave radiation was derived from the data distribution in a histogram and set to 50 W m^{-2} (Figure 2.2). A night was classified as a cold-air night if at least 50% of the nocturnal time fulfilled both criteria.

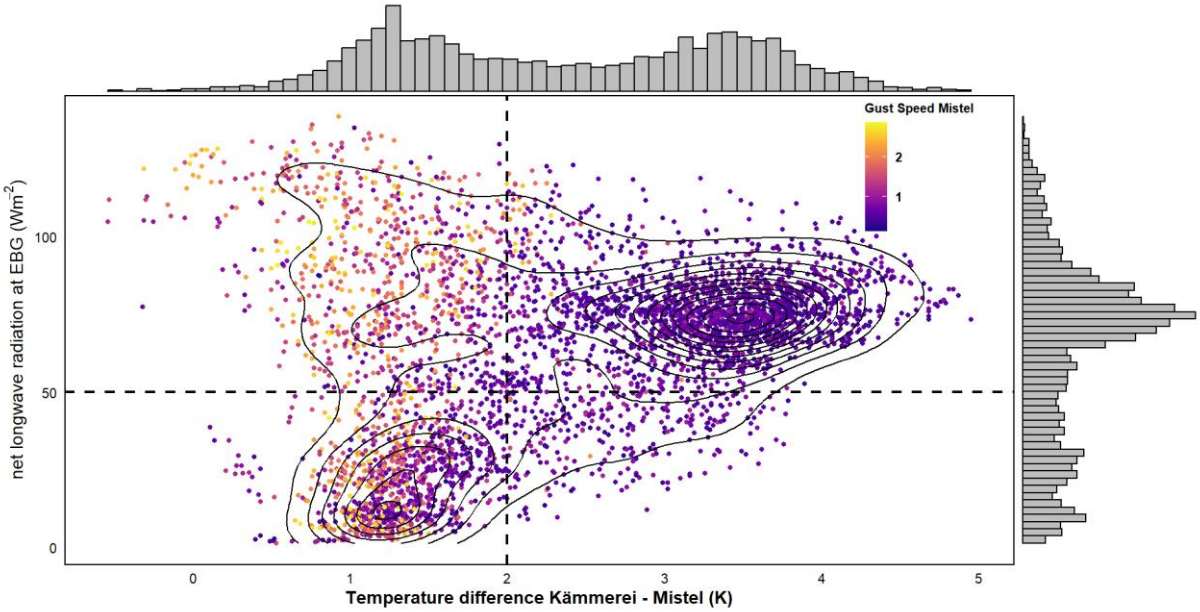

Figure 2.2 The net longwave radiation (outgoing minus reflected from clouds) is shown in dependence of the temperature difference between the MWS Kämmerei and Mistel. The dots are ten-minute intervals (measured at the EBG station, averaged from the five-minute intervals of MWS Kämmerei and Mistel) of all nights in July and August, colour coded according to the 95th percentile of gust speed. Isopleths indicate the density of the data points, while histograms display their distribution. The vertical line indicates the 2 K criterion by Schappacher (2024). The horizontal line represents the threshold of 50 Wm^{-2}, defined on the basis of the histogram distribution.

Tropical nights were classified according to the criterion of the DWD (Deutscher Wetterdienst), which defines them as nights with a minimum air temperature ≥ 20 °C between 18:00 UTC and 06:00 UTC. This was adapted to the chosen timeframe of 18:00 CEST to 06:00 CEST (Deutscher Wetterdienst, 2025a). The criterion was applied to all MWS in the St. Georgen/Burg district to identify tropical nights in general and to assess their distribution across the different research sites.

Nights selected for examining the maximum UHI magnitude were classified according to the following criteria: Eligible nights had to meet the cold-air criterion (see above), and the preceding day was required to be classified as autochthonous according to Spakowski (2025). An autochthonous day in this study is defined by predominantly net outgoing radiative conditions during both day and night, as well as calm wind conditions during the day (< 2.2 m s^{-1}). Autochthonous weather conditions characterized by low cloud cover and weak wind speeds reduce atmospheric mixing and therefore enhance the intensity of the UHI effect. Wind and cloud cover are key factors influencing radiation balance, convection, and advection processes, which in turn drive temperature differences between urban and rural areas (Oke, 1973).

2.1.2 Land use classification

To be able to make more precise statements about the different land use types within the city and their effect on the respective microclimate, the MWS were allocated into three different categories – urban, semi-urban and open spaced (Sungur et al., 2025). The differentiation was based on the phenomenological characteristics of the MWS (Figure 2.3).

Stations		Leersstraße	Retirement home	Correction facility	Allotment Association	Tekirdagplatz	graveyard	Wilhelminenaue	St. Georgen Street
Land Cover Type in %									
	Pavement	85	>95	60	50	100	30	10	90
	Vegetation	15	<5	40	50	0	70	70	10
	Water	0	0	0	0		0	20	0
Building Cover in %		65	60	50	20	80	20	<1	70
Building Arrangement		in row	in row	spread	spread	in row	spread	isolated	in row
Distance to building		1, 7, 18	0, 30, 30	4, 6, 24	34, 45, 86	14, 21, 21	31, 103, 134	88, 134, 135	2, 13, 16
mean distance to building		9	20	11	55	19	89	119	10
data analysis									

Figure 2.3 Classification metric for measurement stations. The eight stations in St. Georgen were allocated after the metrics on the left side to the three microclimatic categories 'urban', 'semi-urban' and 'open-spaced' based on their phenomenological similarities. This classification approach is adopted from Sungur et al. (2025). The yellow marked stations are classified as 'urban', the green ones as 'semi-urban' and the blue one as 'open-spaced' (rural). (Data from Geodaten Bayern, 2025).

2.2 Mobile measurements

To complement the stationary observations, mobile measurements were conducted using an instrumented cargo-bicycle. The objective of this campaign was to capture the spatial variability of climate elements and to map cold-air flows, cold-air accumulation, and flux densities within the urban environment. The case study was performed during a pronounced cold-air night from August 5th to 6th, characterized by synoptic conditions of clear skies with wind speeds of approximately 1 m s^{-1}. During this night, mobile measurements were conducted at 00:00, 02:00, and 04:00 CEST to assess nocturnal dynamics, complemented by an additional ride at 12:00 CEST to capture the transition to daytime heating.

2.2.1 Bike Set up

The cargo bike was equipped with an ultrasonic anemometer, at a measurement hight of 1.6 m and a LI-COR open path gas analyser, at a measurement hight of 1.35 m. The instruments were fixed on a triangle truss on a detachable platform. For positioning and motion data an inertial navigation system (INS) system with two antennas was employed. In addition to GPS data, the INS also records heading and orientation, which are essential for the precise correction of wind direction and flux calculations. All three instruments were connected to a laptop, with the Smartflux3 system, running for the anemometer and the gas analyser, as well as the sbgDataLogger for the INS system. All data were measured in UTC, which later allowed the collected data to be synchronized in time with the corresponding spatial information. Description in more detail can be found in Figure 2.4 and Table 2.3.

The sonic anemometer's north orientation and the INS x-axis were set to the direction of bicycle movement. This configuration facilitated the subtraction of the motion-induced wind component from the measured wind speed and direction. In addition, movement detected by the INS were used to correct the sonic anemometer data, ensuring that the reported wind speed and direction reflect only the atmospheric signal.

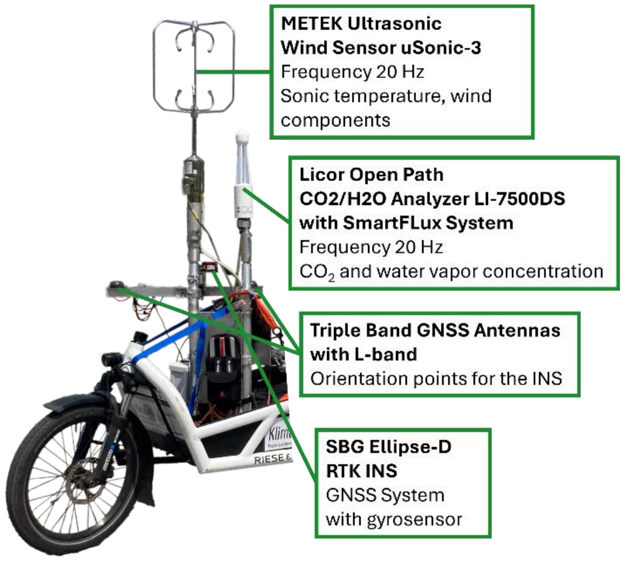

Figure 2.4 Set up of the instruments on the cargo bike.

Table 2.3 Measurement devices with measured parameters equipped on the cargo bike. (LI-COR, 2025; METEK, 2024; SBG Systems, 2025)

Instrument	**Information**	**Measured parameters**
Ultrasonic anemometer	METEK Ultrasonic Wind Sensor uSonic-3 Cage MP with 2-axis inclinometer Frequency 20Hz	Sonic temperature Wind components
Gas Analyzer	Licor Open Path CO_2/H_2O Analyzer LI-7500DS with SmartFlux3 System Frequency 20Hz	CO_2 concentration water vapor concentration
GNSS system and Gyro sensor	SBG Ellipse-D RTK INS with triple band GNSS antennas with L-band	Position, heading, alignment
Logger	Laptop with Smart flux 3 system	
Energy supply	Power banks, Dino Kraftpaket	

2.2.2 Route

The course of the measurement route combined with the placement of the MWS was intended to capture the spatial heterogeneity of the urban environment. The route had a length of approximately 10 km and covered an area of about 2.5 km^2. With a speed of around 4 to 6 m s^{-1} one measurement ride took about an hour. During the ride, the bike was stopped for approximately two minutes at each MWS. This allowed for a direct comparison between mobile measurements and the corresponding stationary data, as well as an assessment of potential differences between measurements taken while stationary versus in motion.

The measurement route started at BayCEER in the northern part of St. Georgen and headed south through part of the industrial area to the first MWS at Leersstraße, located within a detached built residential area. After the stop, the route continued west through more residential zones to the retirement home, situated next to a construction area and a major street. The next stop was at the correction facility, reached after riding south through more residential areas and a main street. From there, the route proceeded west to the allotment association, following a bikeway shaded by trees. Afterwards, it passed through further residential areas and two main streets (Markgrafenallee and Brandenburger Straße) to Tekirdagplatz. From there, the route turned east along a bikeway bordered by trees and a meadow adjacent to the graveyard, followed by more vegetated residential areas leading down to the Wilhelminenaue floodplain. On the way back north, the route crossed less densely built residential areas with more garden spaces, passed along the cemetery, and continued through the main street of St. Georgen with dark cobblestone pavement and densely built houses, before returning via Leersstraße to BayCEER (Figure 2.5).

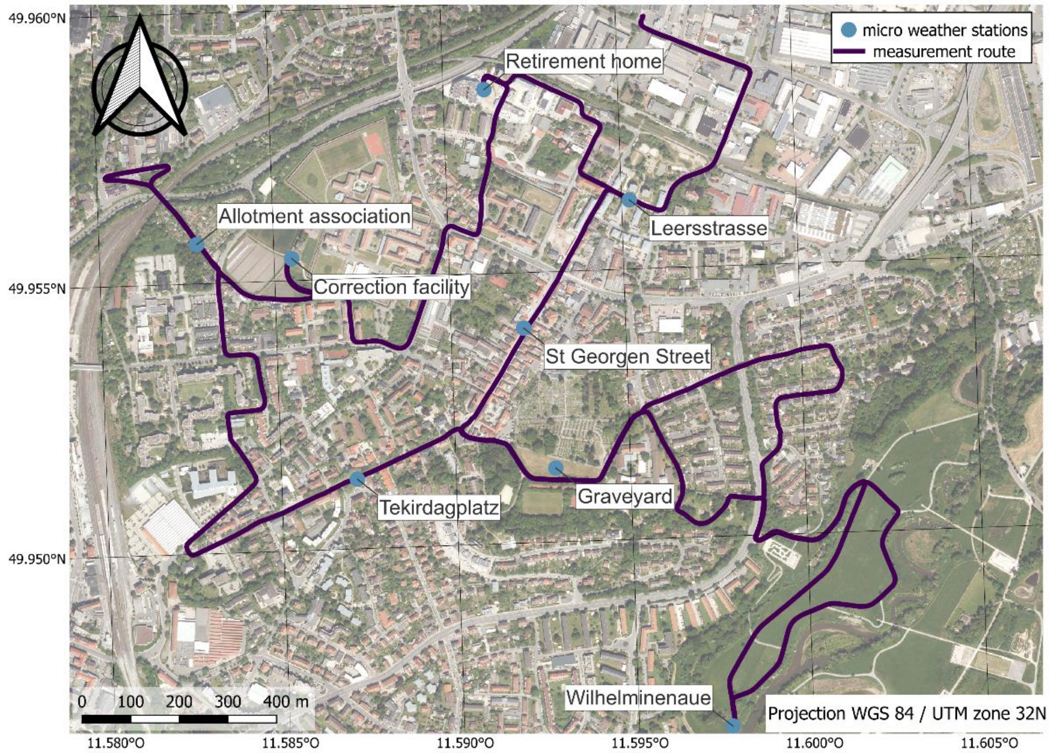

Figure 2.5 Measurement route and micro weather stations along the route in St. Georgen/Burg.

2.2.3 Post processing of observations

For the processing of the mobile measurement rides, including the calculation of motion-corrected flux densities and turbulent statistics, the software bmmflux, version v8p4, developed by C. K. Thomas, was employed. To ensure data quality, several corrections and filtering procedures were applied. For flux calculations, the motion-corrected sonic anemometer wind vectors were rotated into the principal streamline of the uncorrected INS data, aligning the measurements with the main wind direction and ensuring that the mean vertical wind component was zero. In addition, a spectral correction was applied to the high-frequency range following the method of Moore (1986), and calculated frequency correction factors greater than 1.5 were filtered out to avoid overestimation of turbulent fluxes. Additionally, data with a beta rotation angle, which indicates the tilt, above 15° were filtered out. These preprocessing steps ensured that the resulting fluxes and turbulence statistics accurately reflect atmospheric conditions, corrected for the motion of the mobile set up.

As the ultrasonic anemometer measures the sonic temperature T_{sonic}, which can be approximated with the virtual temperature, the air temperature had to be calculated via the specific humidity (Equations (2.3) and (2.4)).

$$T_{air} = \frac{T_{sonic}}{1 + 0.608 \cdot q} \tag{2.4}$$

(Foken & Mauder, 2024a)

For comparability of the measured temperature and vapor pressure along the one-hour ride, the data had to be temporally and spatially detrended. For temporal detrending a point in time close to the mid-time of the measurement ride was chosen according to which the relative air temperature within the time frame of the measurement ride of all MWS (except GY) was calculated. The GY station was excluded because of its location on the open meadow next to the bikeway, while the bikeway is lined with a treeline. Furthermore, the relative values were brought to 2 s resolution by "nearest neighbour”. After that the mean of all relative MWS air temperatures was subtracted from the air temperature of the ride. For spatial detrending an inverse square distance weighted correction value for every single measurement value was calculated. Firstly, the distance between every measured data point and every MWS was calculated, secondly a relative weighting to all relative values of the MWS for each time step dependent on the distance was prescribed. Then all relative values with their respective weighting were summed up and subtracted from the raw measurement value. As structured in Equation (2.5).

$$Value_{corrected} = Value_{raw} - \sum_{i=1}^{7} \frac{\frac{1}{d_i^2}}{\sum_{j=1}^{7} \frac{1}{d_j^2}} \cdot r_i \tag{2.5}$$

(Babak & Deutsch, 2009)

1-7: number of MWS

d: distance [m]

r: relative value [°C / kPa]

The absolute wind directions $\varphi_{corrected}$ were calculated by adding the yaw provided by the INS φ_{yaw} to the measured relative wind directions of the anemometer $\varphi_{measured}$ (2.6). Wind speeds <0.5 m/s were excluded from the wind direction analysis because under calm conditions, wind direction becomes highly variable and does not represent a consistent flow pattern.”

$$\varphi_{corrected} = (\varphi_{measured} + \varphi_{yaw}) \cdot mod(360) \tag{2.6}$$

To fulfil the steady state conditions of Eddy Covariance during the motion, homogeneous street transects were defined (Figure 2.6). Along these transects no influence of crossroads was expected and the building and vegetation is invariant, which allows to assume steady state conditions. To stay within these transects a perturbation time of 32 s is chosen, which will underestimate the actual flux density as the lower frequency proportion of the fluxes is missed for short sampling times (Foken & Mauder, 2024b). Assuming a constant distribution of the turbulence eddy sizes for the whole study area, the calculated fluxes can still be used to compare differences in flux densities between the different transects. The land use transects were chosen after the classification of the MWS (Figure 2.3), combined with an on-site assessment and inspired by Žgela et al. (2024). The transects were graded into residential areas with and without treeline, main streets with and without treeline, green corridors, meadow/floodplain, square with trees and crops/meadow (Figure 2.6).

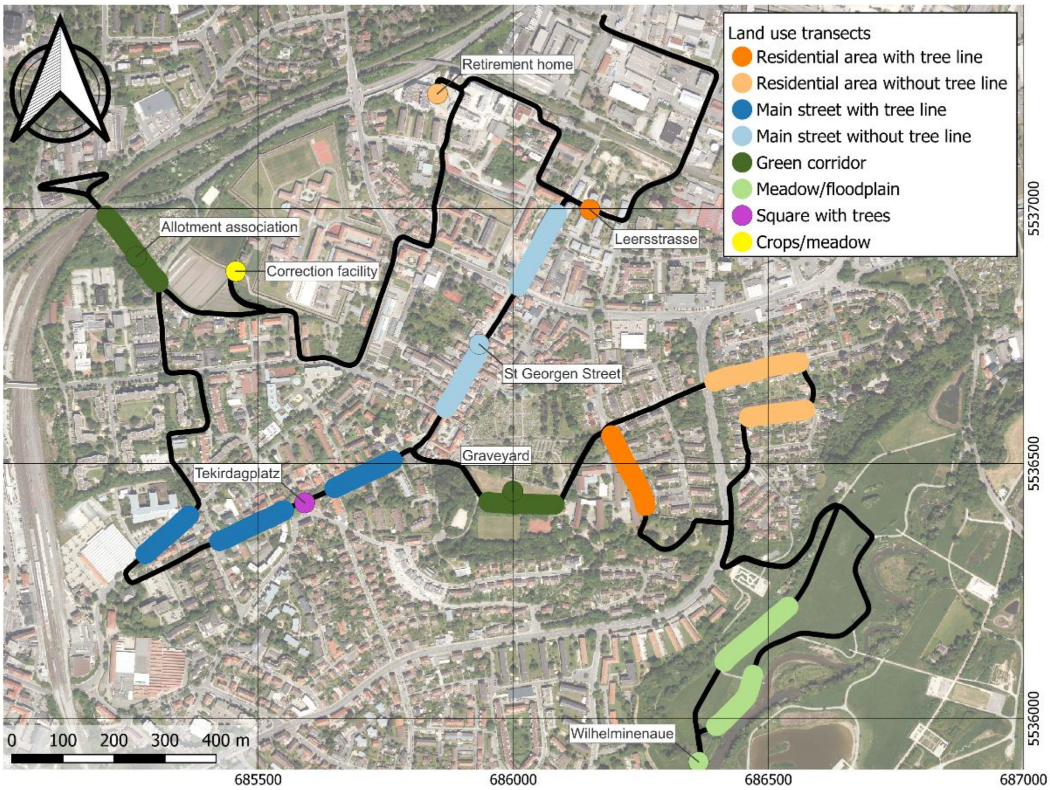

Figure 2.6 Measurement route and MWS in St. Georgen/Burg with categorized homogeneous transects. The transect categories were inspired by Žgela et al. (2024) and changed to fit the research area. Projection: ETRS89 / UTM zone 32N

A complete eddy covariance analysis requires a spectral analysis of the (co)variances. Spectral analysis is applied by decomposing time series data into their frequency components via Fourier transformation. The power spectra of single signals and the cospectra of vertical wind with variables are of particular interest, as they represent the distribution of variances and covariances across different frequency bands. Since the integral of a (co)spectrum equals the (co)variance of the original signal, spectral analysis is a key tool for evaluating flux contributions and potential losses at different scales (Aubinet et al., 2012). The methodology applied here follows the theoretical framework of Taylor (1938), Kaimal & Finnigan (1994) and the practical guidelines of Foken & Mauder (2024).

With a perturbation time of 32 seconds the actual flux densities will be underestimated as the low frequency proportion of fluxes is missed, but a comparison between differences in flux densities between the different transects should be possible.

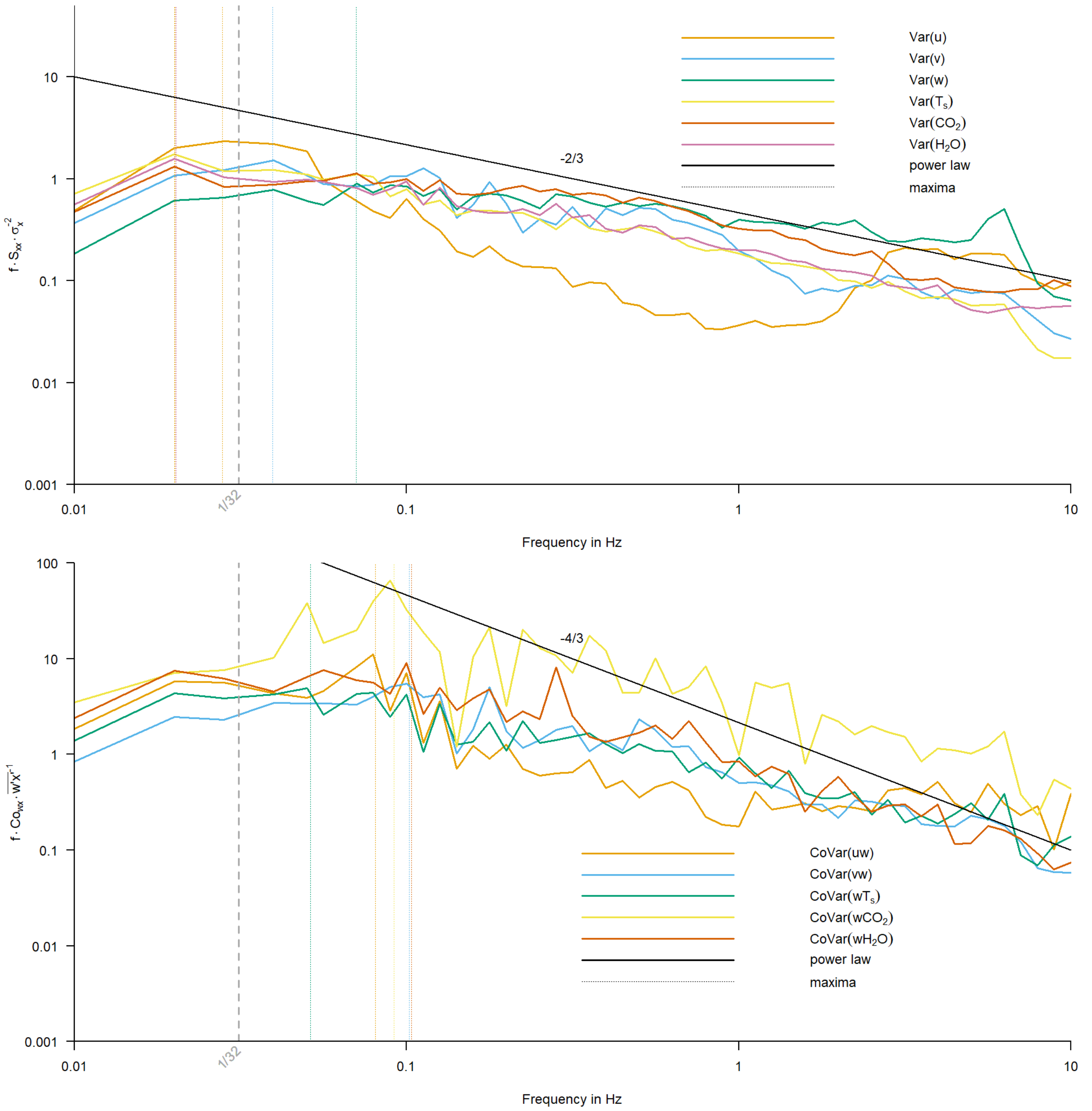

Figure 2.7 Normalized and frequency normed mean power- and co-spectra for Eddy Covariance analysis of the three measurement rides with a perturbation time of 52 s. Top: Power spectra of the vertical wind variance (Var(w)), variance of wind component 'v' (Var(v)), variance of wind component 'u' (Var(u)), sonic Temperature variance (Var(T_s)), variance of absolute humidity (Var(H_2O)) and variance of CO_2 (Var(CO_2)). Bottom: covariance of the wind components 'w' and 'u' (CoVar(uw)), covariance of the wind components 'v' and 'w' (CoVar(vw)), covariance of the vertical wind and the sonic temperature (CoVar(wT_s)), covariance of the vertical wind and CO_2 (CoVar(wCO_2)) and covariance of the vertical wind and absolute humidity (CoVar(wH_2O)).

3. Results

During the research period in July and August 2024, a range of different weather conditions occurred, although the months were predominantly characterized by warm temperatures and frequent high-pressure systems (Table A.1). At the EBG tower, air temperature varied between 7.9 °C at the end of August and 33.4 °C in mid-August, while at the SG station values ranged from 9.7 °C to 34.1 °C (Figure 3.1). Within this period, a total of 33 cold-air nights, three tropical nights, and seven 'UHI' nights, defined as autochthonous days followed by cold-air nights, were identified (Figure 3.2).

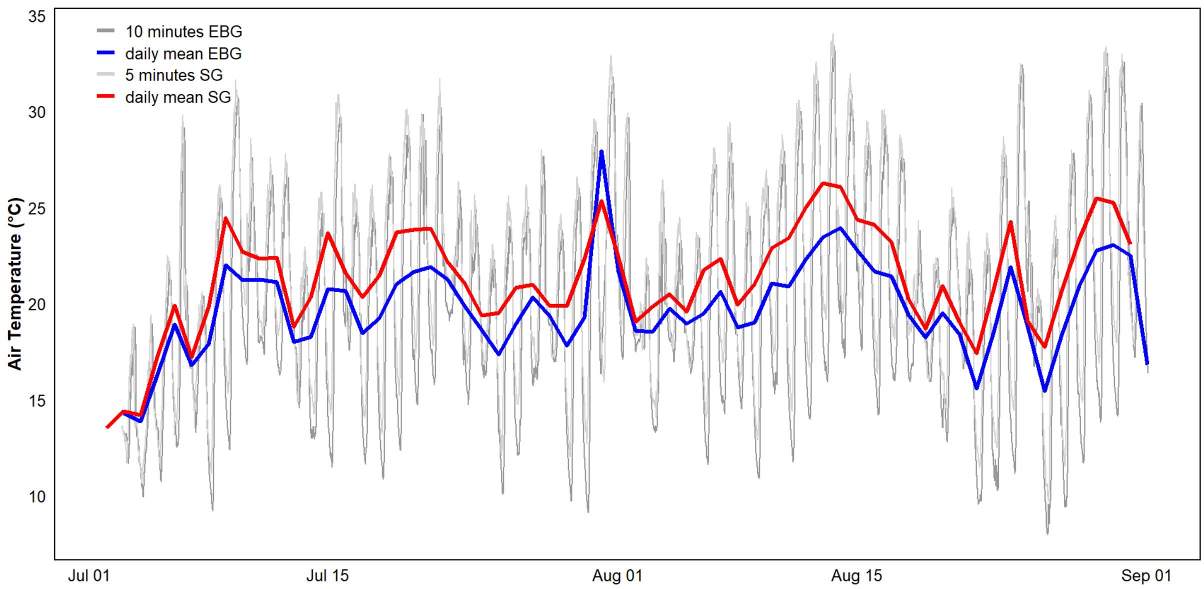

Figure 3.1 Time series of air temperature at EBG (blue) and SG (red) from July 3rd to August 31st. A data gap at EBG from July 30th 23:50 until July 31st 11:00 occurred, which explains the high daily mean temperature on July 31st.

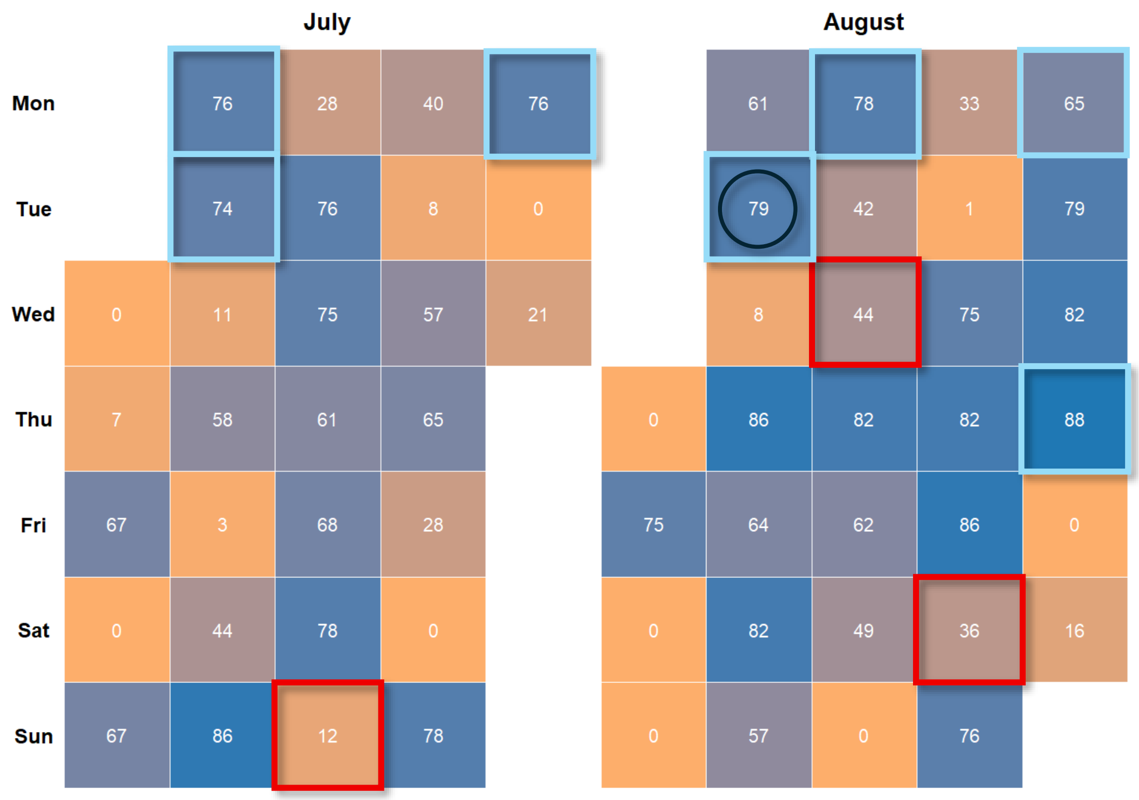

Figure 3.2 Duration of cold-air night conditions per night, expressed as percentages, during the measurement period from July 3rd to August 31st, 2024 (orange to blue scale). Nights with at least 50% of the measurement intervals fulfilling the criteria were classified as cold-air nights. Tropical nights are marked in red, and "UHI" nights (autochthonous day + cold-air night) are marked in light blue. The morning of the cold-air mobile measurement ride is circled in black. The classification follows the definitions provided in Chapter 2.2.1.

3.1 Cold air and radiation nights

To give an overview over the 33 cold air nights during the measurement period and the variability of temperature within the city, the temperature of the five-minute intervals of every station was averaged to ten minutes in order to calculate the temperature difference to the EBG station. To compare differences between cold air nights and non-cold-air nights mean diurnal courses of air temperature were calculated following the classifications (Figure 3.3 and Figure 3.4).

Larger differences between the stations indicate distinct microclimates, especially during night. The urban classified stations plus the CF station tend to temperature differences throughout 3-4 K during cold air nights, while the semi-urban GY and AA stations show temperature differences around 1-2 K (Figure 2.1). This effect can still be observed during non cold-air nights, but with smaller temperature difference amplitudes. The urban stations are 2-3 K warmer than the EBG station, while GY and AA stations are around 1 K warmer (Figure 3.4).

Strong temperature differences between the stations occur between 22:00 and 06:00 CEST. During daytime the temperatures draw closer to each other, not showing the differences in land use, which can be observed during night. The peak of the UHI established around 21:00 CEST during cold air nights as well as non-cold air nights, right after a steep increase of the temperature difference. Afterwards the temperature difference decreases and stays around 1 K below the peak.

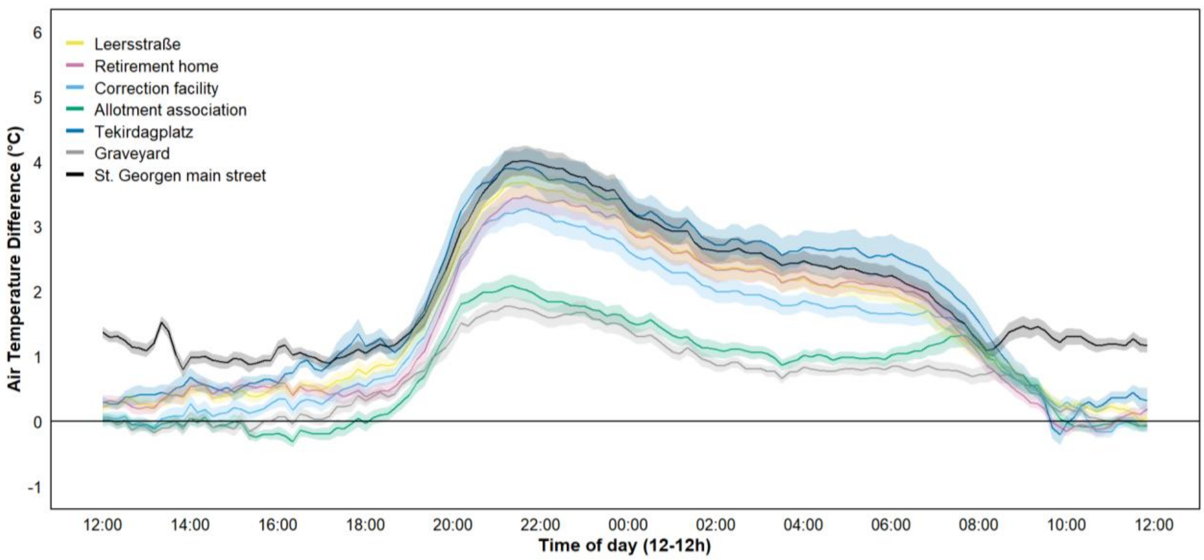

Figure 3.3 Mean diurnal course of air temperature difference at the MWS (station – EBG) with standard error during cold air nights (n=33) within the measurement period. The shown time frame is 12:00 CEST of the given day in Figure 3.2 until 12:00 CEST the next day.

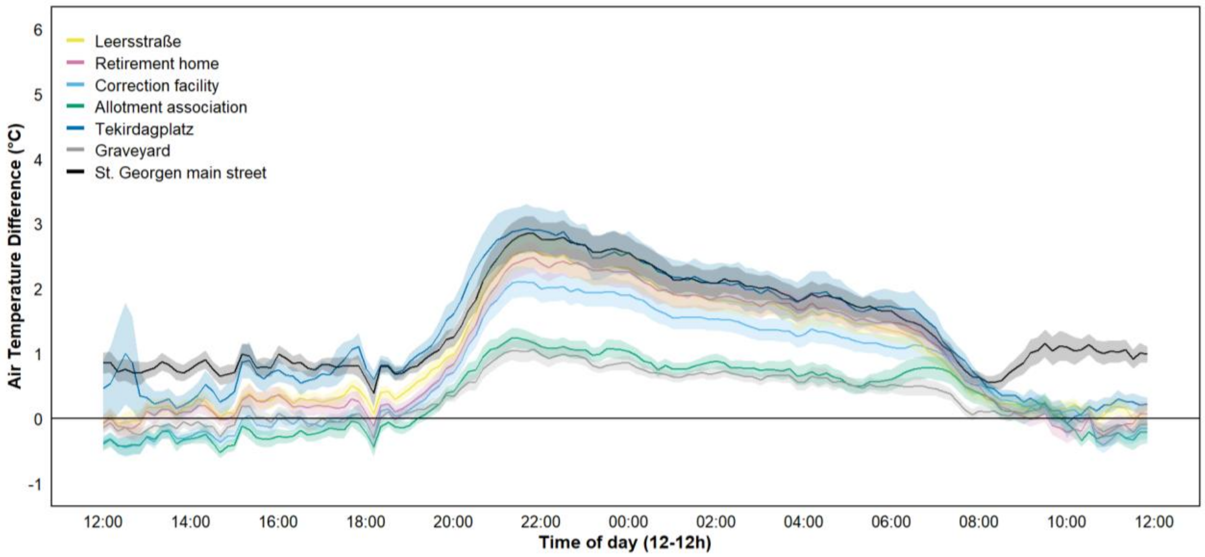

Figure 3.4 mean diurnal course of air temperature difference at the MWS (station – EBG) with standard error during non-cold air nights (n=27) within the measurement period. The shown time frame is 12:00 CEST of the given day in Figure 3.2 until 12:00 CEST the next day.

3.2 Urban heat island in St. Georgen/Burg

To investigate the maximum development of the UHI, the 33 cold-air nights were further filtered to include only those preceded by autochthonous days, representing periods with minimal mesoscale transport. These seven selected days will be labelled as 'UHI-days' in the following.

With the MWS distributed over the research area, the UHI effect could be analysed spatially and temporally. For the nighttime strong mean differences in temperature were found. The average UHI for the stations is up to 4-5 K during the night (Figure 3.5). In general, stations in more densely built, urban areas were warmer than the one in vegetated, open spaced sites. To show the measured heat variability the daily mean of the air temperature was calculated for a 24 h interval. During the whole night the station at the St. Georgen Street was warmest. Two groupings can be observed, one with the urban classified stations including the station at the correction facility, the other two remaining semi-urban stations GY and AA. The urban and CF stations show UHI values between 2.5 and 5 K, whereas the semi-urban stations are only 1 to 2 K warmer than the rural reference EBG. The highest temperature difference appears around 21:00 CEST after a steep increase and lowers during the night until a strong decrease in the morning between 6:00 and 10:00, when the stations temperatures converge to the air temperature at EBG (Figure 3.5).

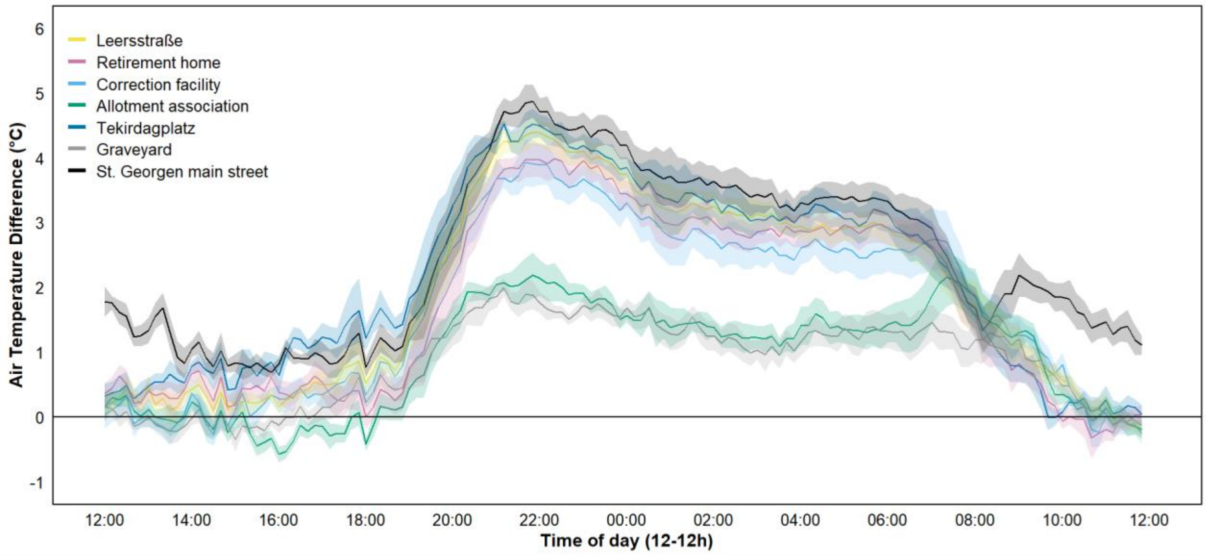

Figure 3.5 Mean diurnal course of air temperature difference (station – EBG) with standard error on UHI-days (n=7) during the measurement period Jul 3rd to Aug 31st, 2024.

Besides the seven days selected to examine the UHI effect, three tropical nights occurred during the measurement period. One night in July (21st) and two nights in August (14th and 24th) (Figure 3.6). These showed three very different synoptical courses. The first two tropical nights were quite typical with warming in the next morning, while the morning after the 24th continued to cool further down, even below the 20 °C threshold (Figure 3.6).

The temperature course on July 21st exhibited cooling in the afternoon, followed by a slight warming around 20:00 CEST, while during the rest of the night the temperature remained nearly constant around 20 °C. The GY and AA stations fell below 20 °C around 02:00 CEST, thus excluding their measurement location from the tropical night classification. According to the DWD criterion all other stations were therefore classified as tropical nights. However, at 10:00 CEST most stations (except LS, RH, and SG) briefly dropped below the 20 °C threshold during the onset of the morning warming (Figure 3.6).

The temperature course of August 14th shows a constant cooling during the whole night. With the stations LS, RH, TP and SG fulfilling the tropical night criterion. However, the stations LS and RH drop below 20 °C at 07:00 CEST. Again, GY and

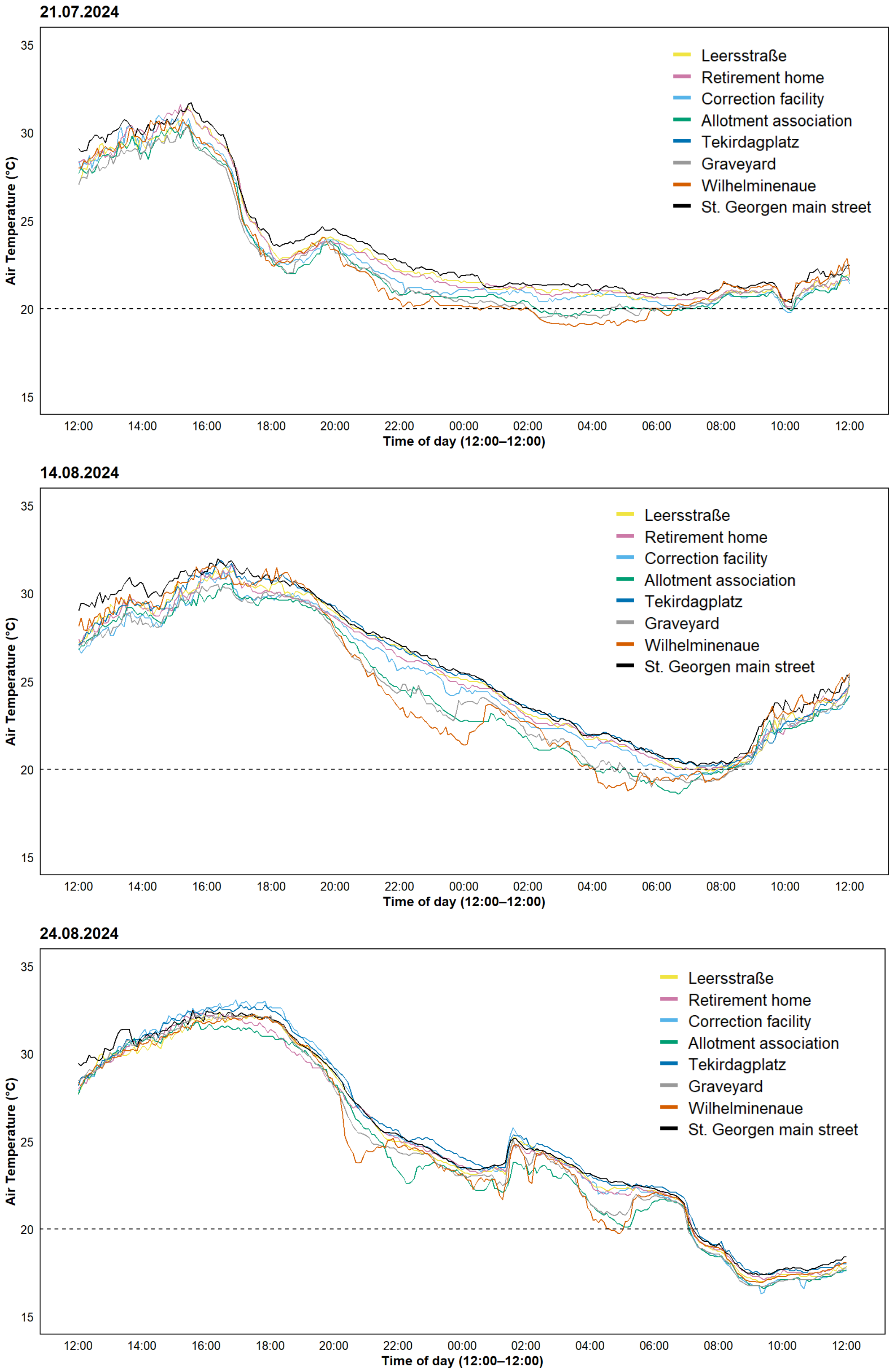

Figure 3.6 diurnal course of air temperature during the three tropical nights. The x-axis showing the time of the day from 12:00 to 12:00 CEST, the y-axis showing the air temperature with a dashed lined at 20°C, which is the threshold for being classified as tropical night.

AA are shown to be the coldest stations with approximately 1-2 K temperature difference to the next coolest station CF (Figure 3.6).

The temperature course of August 24th shows a constant cooling until 01:00 CEST, followed by a temperature increase of ca. 1-2 K. From there the temperature decreased constantly again until around 07:00 CEST, where it rapidly dropped below the 20°C threshold, further indicating advection of cold air (Figure 3.6).

During all nights the temperature course of the MWS is very similar, GY and AA are respectively the coldest stations, which dropped beneath 20 °C every night, but still do not show much difference to the other stations. The net longwave radiation at EBG is presented in the appendix (Figure A. 10 and A. 11).

3.3 Early morning transition and warmup rate

The heating rate was calculated as the slope between two measured values and added up to an hourly value. The here represented data shows the mean diurnal heating rate per station the morning, 04:00 to 12:00 CEST, after the 33 cold air nights. For comparison the heating rate of the remaining 27 mornings is attached in the appendix (Figure A. 12).

Directly after sunrise the rural and semi-urban classified stations exhibit heating rates approximately 1 K h^{-1} higher than those of the urban ones. The TP station shows a 0.5 K h^{-1} lower heating rate compared to the other urban locations. The order of stations reaching their maximum heating rate is as follows: GY, CF, EBG/LS, SG, AA, TP, RF. The earliest peak occurs at GY at 08:00 CEST, whereas RF reaches its maximum latest around 10:10 CEST. By 09:00 CEST, approximately three hours after sunrise, all stations converge at a heating rate of ~2.5 K h^{-1}. TP and RH achieve their maxima slightly later, and by 12:00 CEST, all stations display comparable heating rates again, at around 1.5 K h^{-1}.

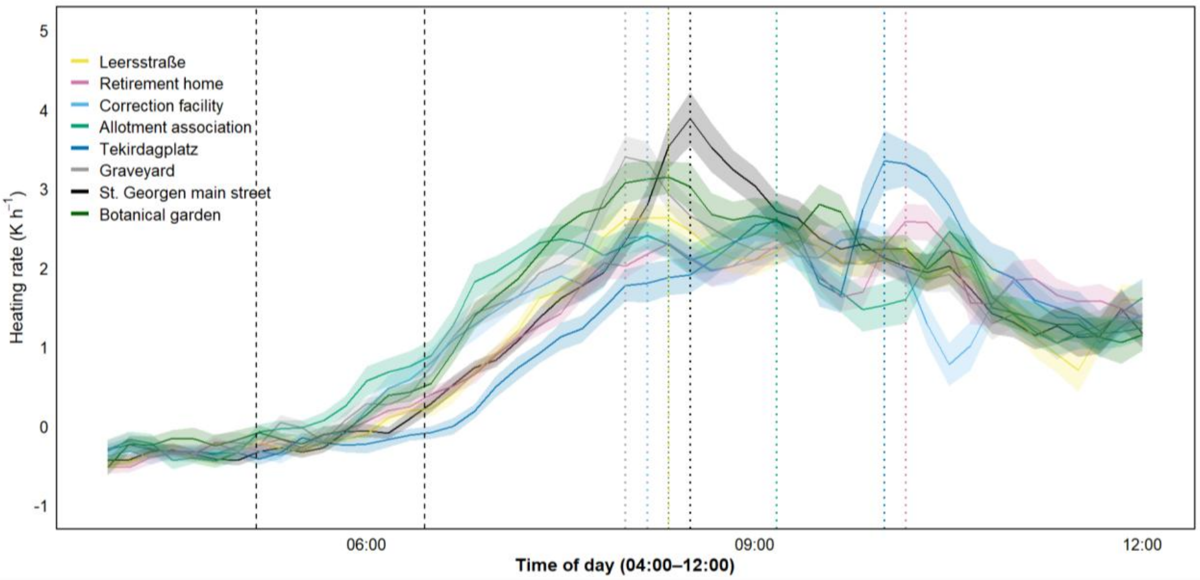

Figure 3.7 Mean diurnal course of the morning heating rate of all stations between 04:00 and 12:00 CEST with standard error after the 33 cold air nights. The dashed lines show the time frame of the sunrise during the research period. The dotted lines in the respective colour indicate the point of maximum heating rate for each station.

3.4 Cold air influence in St. Georgen/Burg with cold air flows and accumulation

To assess microclimatic variability, spatially continuous mobile measurements were conducted in the St. Georgen/Burg district. These measurements allowed for investigation of spatial variations in temperature and humidity at the street-canyon scale. During the measured cold air night (August 06th), the three rides at 00:00, 02:00 and 04:00 CEST showed overall cooling during the night (Figure 3.8). Within the measurement rides the temperature difference reached up to 5 K between different transects. The results presented here are based primarily on the 02:00 CEST measurement, as it provides the only complete dataset of the entire campaign. Data from the two remaining rides are included for comparison (Figure 3.8 and Figure 3.11), with additional visualisations available in the appendix (Figures A.11–A.14).

The air temperature along the urban, denser parts shows a narrow amplitude of around 1 K during the ride. There are three locations where the temperature drops distinctly below the mean temperature of the ride. These are around the AA, the GY and most strongly developed in the Wihelminenaue. These three areas reach temperature differences down to -2.5 K at Wilhelminenaue. The residential areas between RH and CF as well as the residential areas in the east show values close to the mean temperature, which is 15.0 °C for this ride. The warmest route section is in the St. Georgen main street with 2.3 K above the mean temperature of the ride, followed by the transects of Brandenburger Straße and Markgrafenallee in the southwest, showing temperature differences of around 1 K above the mean (Figure 3.9).

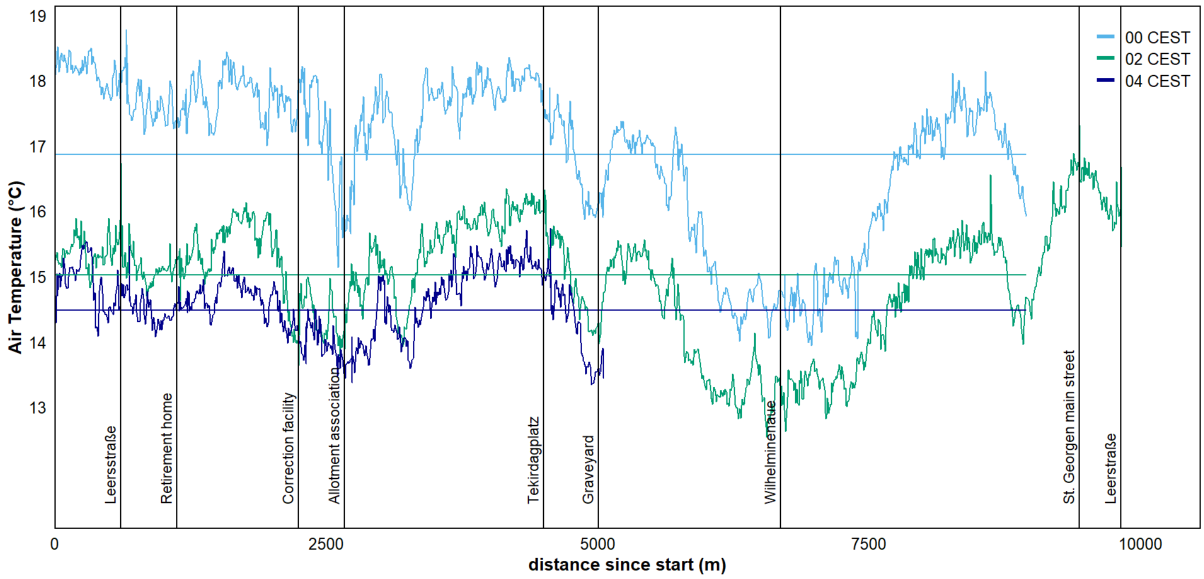

Figure 3.8 Spatially and temporally detrended and corrected air temperature during the three measurement rides. The x-axis represents the distance from the starting point, calculated using the haversine formula to account for the Earth's curvature. In addition, the stopping points next to the MWS stations are marked. The y-axis shows the air temperature, with horizontal lines in corresponding colours indicating the mean temperature of each ride.

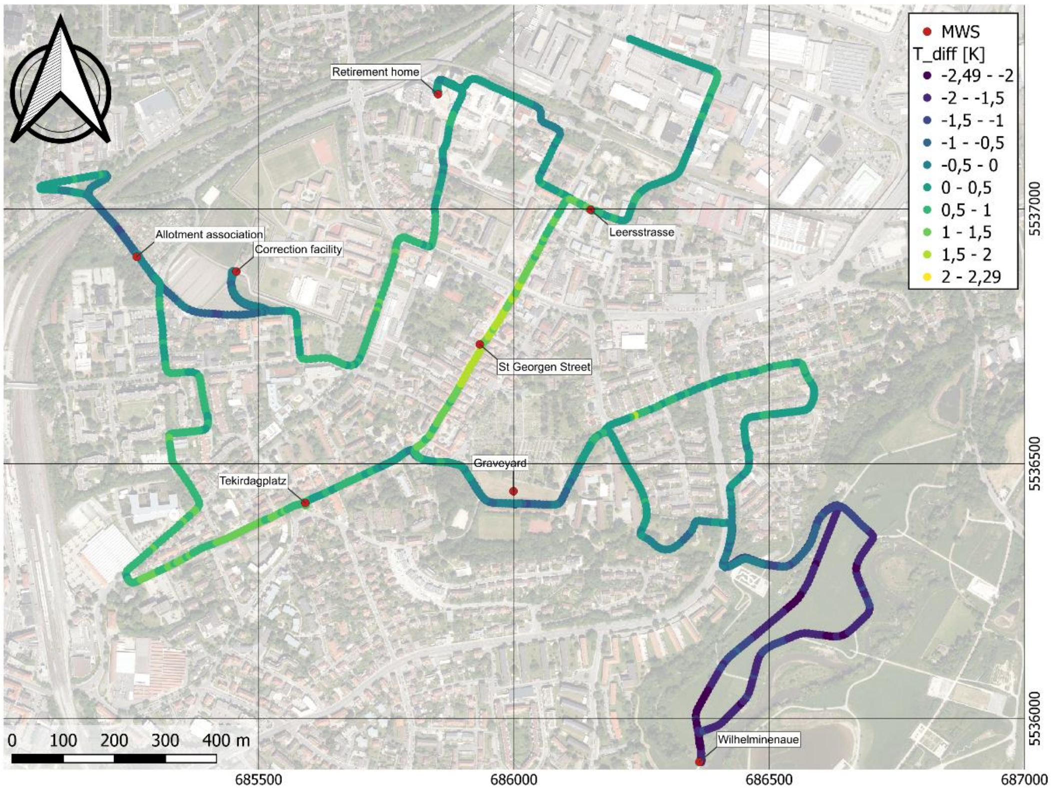

Figure 3.9 Deviation from mean corrected air temperature during the ride 02:15 – 03:30 CEST, detrended to 03:00 CEST; projection: ETRS89 / UTM zone 32N.

The vapor pressure along the route shows differences from the mean with an amplitude of 0.1 kPa. Higher values are in the residential area between RH and CF, as well as along the half open area between CF and AA and down the bike path to the Wilhelminenaue within the residential part. The lowest values appear in the Wilhelminenaue, around TP and SG (Figure 3.10). The mean vapor pressure of this ride is 1.38 kPa. During the night, nearly saturated conditions at the rural and semi-urban stations mainly reflect cooling, which lower air temperature and thus reduce the saturation vapor pressure. This leads to relative humidity values close to 100% even in the absence of active evapotranspiration. In contrast, at the urban sites TP and SG, relative humidity remained around 70%, a result of higher nocturnal temperatures and reduced cooling efficiency, which decrease the relative humidity and thereby prevent saturation despite comparable vapor pressures. Over the course of the night, relative humidity increased, showing higher values during the 02:00 ride compared to the 00:00 ride. In contrast, the differences between 02:00 and 04:00 were less pronounced and in some cases relative humidity remained nearly constant (Figure 3.11).

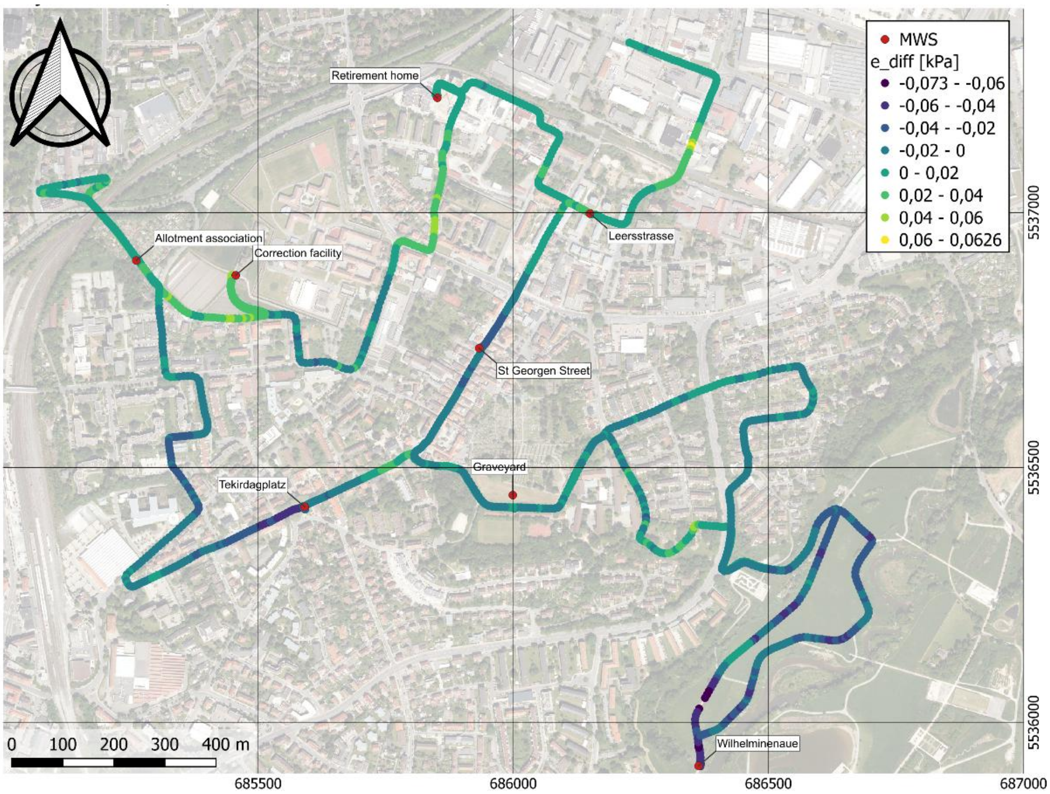

Figure 3.10 Deviation from mean vapor pressure during the ride 02:15 – 03:30 CEST, detrended to 03:00 CEST; projection: ETRS89 / UTM zone 32N

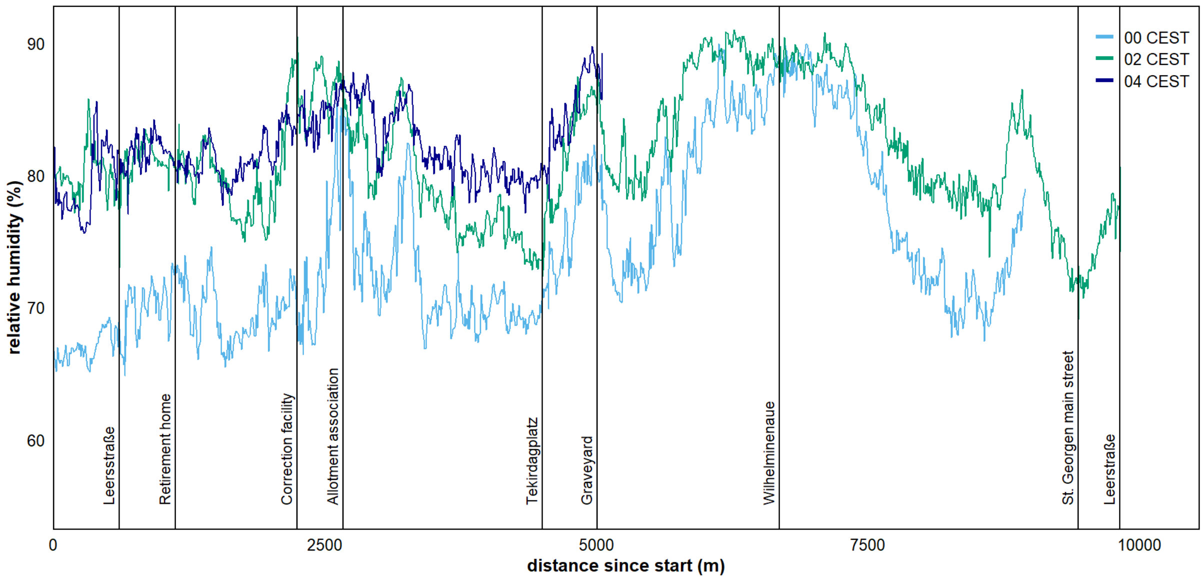

Figure 3.11 Relative humidity during the three measurement rides, calculated with the corrected and detrended air temperature and vapor pressure. The x-axis represents the distance from the starting point, calculated using the haversine formula to account for the Earth's curvature. In addition, the stopping points next to the MWS are marked. The y-axis shows the relative humidity of the three rides.

During the 02:00 CEST measurement, wind directions generally followed the orientation of the street canyon, constrained by houses and trees. At stations located in more open areas (RH, CF, TP, GY, LS), higher wind speeds were observed (Figure 3.12). At intersections, more variable wind directions appeared, particularly at the crossing of Brandenburger Straße, St. Georgen Street, and the bike path to GY, as well as near TP and along Federal Highway 2, which had to be crossed en route to Wilhelminenaue. In the more open area at Wilhelminenaue, the wind was less constrained by pathways and mostly aligned with the valley, from northeast to southwest. The wind measured at the WA station was predominantly from the northwest.

In the Wilhelminenaue, several gaps within the arrows occur due to wind speeds below 0.5 m s^{-1}, particularly along the upper path. Along this section, the prevailing wind direction is oriented parallel to the path, running from northeast to southwest along the depression. In contrast, on the lower and more eastern path, the wind direction shows a more pronounced west–east orientation, following the topography of the valley down to the waterbody.

Further vector maps of the two other measurement rides and wind roses of the other MWS are provided in the appendix (Figure A. 15, A. 16, A.17).

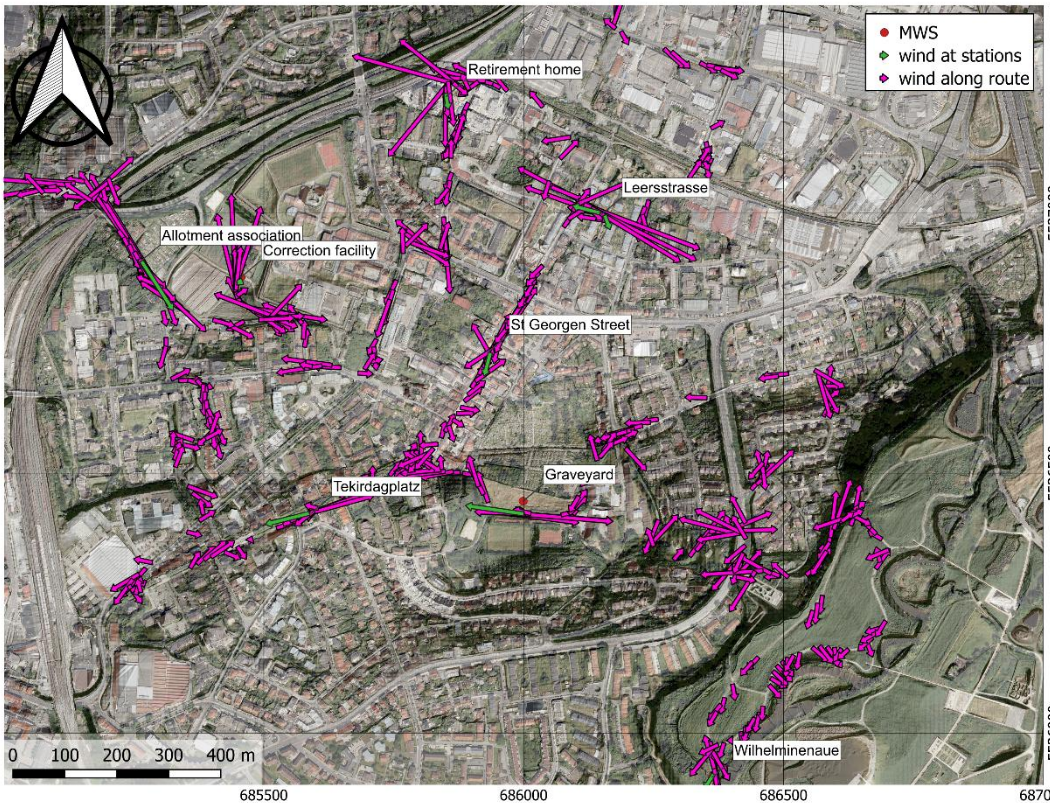

Figure 3.12 wind vectors of direction and speed along the measurement route on a map with relief shading (with z-factor 10) during the ride 02:15 – 03:30 CEST. Only data with windspeed > 0.5 ms^{-1} were used. The maximal windspeed during this ride was 4.7 ms^{-1}. The data were averaged over 4 second intervals, while for each station a mean over the complete stop was calculated. Along the route, the measurements are shown as blue arrows, and the station means are indicated with green arrows. Projection: ETRS89 / UTM zone 32N

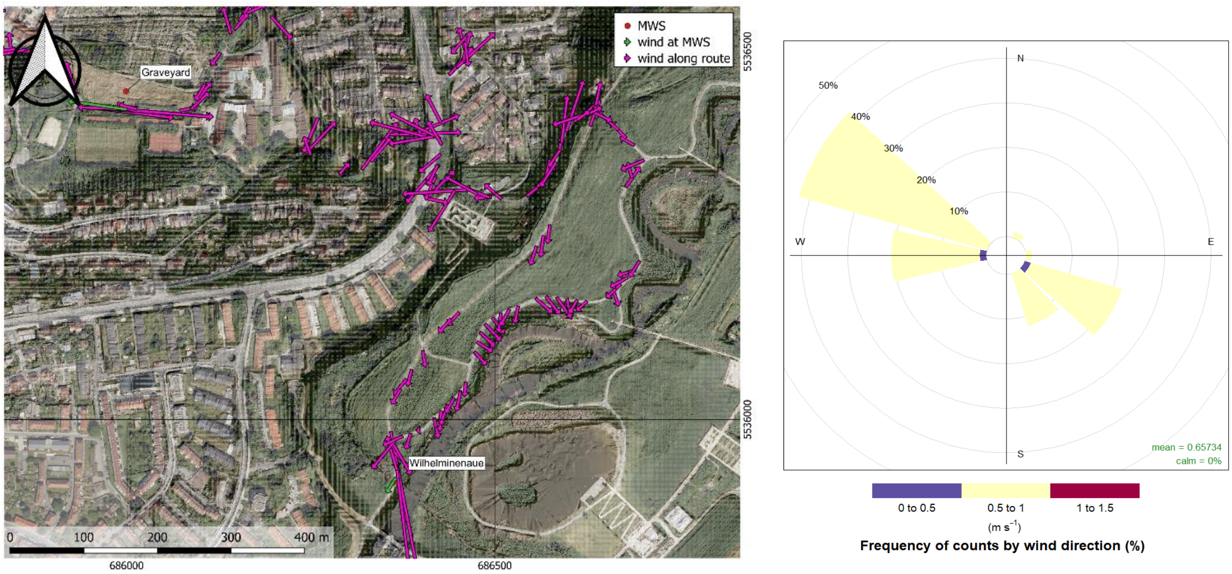

Figure 3.13 14 Left: zoomed-in map of Wilhelminenaue of Figure 3.13. Projection: ETRS89 / UTM zone 32N. Right: wind rose of the MWS WA on 06 August from 00:00 to 06:00 CEST, showing the frequency of wind directions, with wind speed indicated by colour coding.

3.5 Flux densities during the mobile measurement

For presenting the calculated flux densities from the measurement ride during the cold air night, the land use transects presented above are used to colour code the measured fluxes per transect according to their land use as shown in Figure 2.6. The fluxes presented here have to be regarded in comparison to each other, due to the short perturbation time.

At 02:00 CEST, the sensible heat flux shows differences between land-use types along the measurement transect. Positive fluxes were predominantly observed in built-up areas, with the highest values exceeding 20 W m^{-2} in the main street locations (SG, Markgrafenallee and Brandenburger Straße) as well as in residential areas. In contrast, negative or near-zero fluxes occurred at vegetated sites such as meadows, the green corridor, and particularly the Wilhelminenaue floodplain, indicating radiative cooling and weak turbulent exchange, as a negative sensible heat flux reflects a downward heat transfer, occurring when radiative cooling cools the surface below air temperature; under weak turbulence this imbalance persists, producing localized negative sensible heat flux. The AA station and surrounding green areas also showed fluxes close to zero, reflecting their vegetated character. Overall, the spatial distribution shows some contrast between urban surfaces, which continued to release stored heat into the atmosphere, and vegetated surfaces, where cooling dominated during the night (Figure 3.14).

The latent heat flux at 02:00 CEST shows differences ranging between -10 and +10 W m^{-2} along the measurement transects. Stronger positive fluxes were predominantly observed along the mobile transects at Brandenburger Straße and the bikeway, as well as in the St. Georgen main street and at Tekirdagplatz. Some stationary measurements next to the WA station also showed relatively high values. In other land-use types (residential areas without tree lines, meadows, croplands, and the green corridor), fluxes were predominantly negative or near zero. The mobile transects in the Wilhelminenaue in particular exhibited stronger negative latent heat fluxes (Figure 3.15).

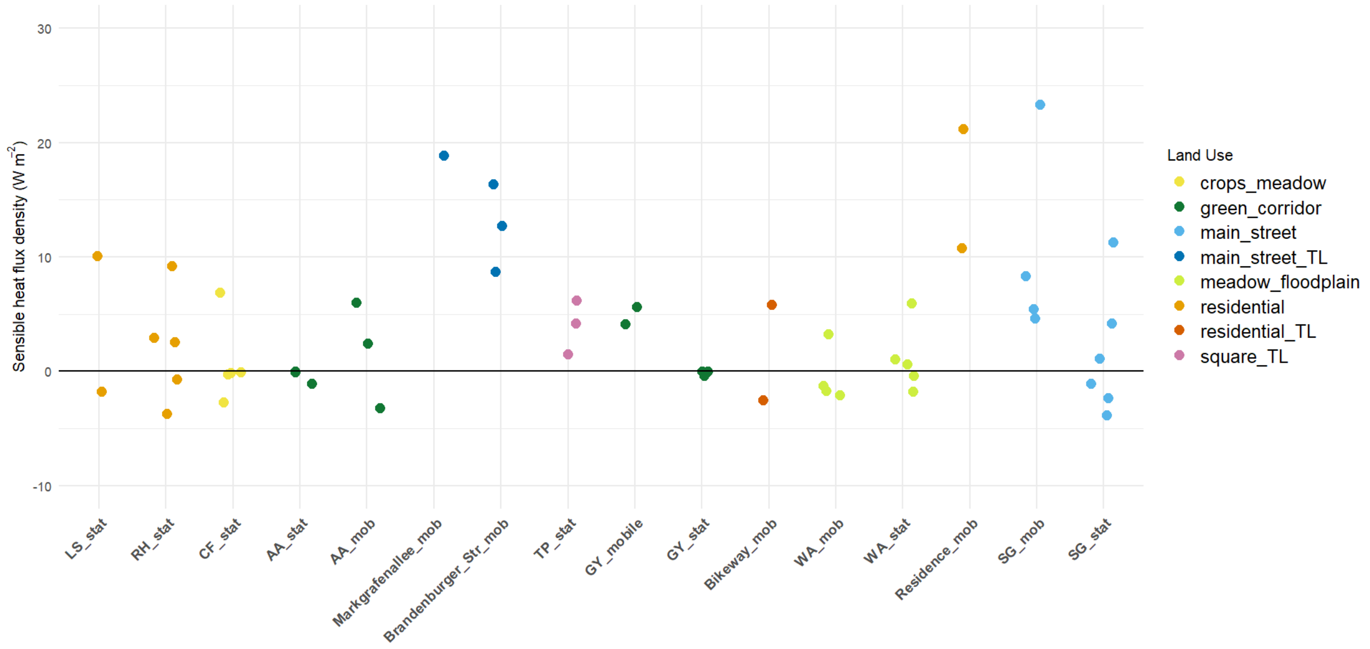

Figure 3.14 Sensible heat flux densities at the 02:00 CEST measurement ride. The x-axis shows the different locations along the measurement route, marked with ‘stat’ for a stationary measurement, where the bike was parked, and with ‘mob’ for a mobile measurement, recorded while riding. The data points are colour coded according to the land use classifications shown in Figure 2.6.

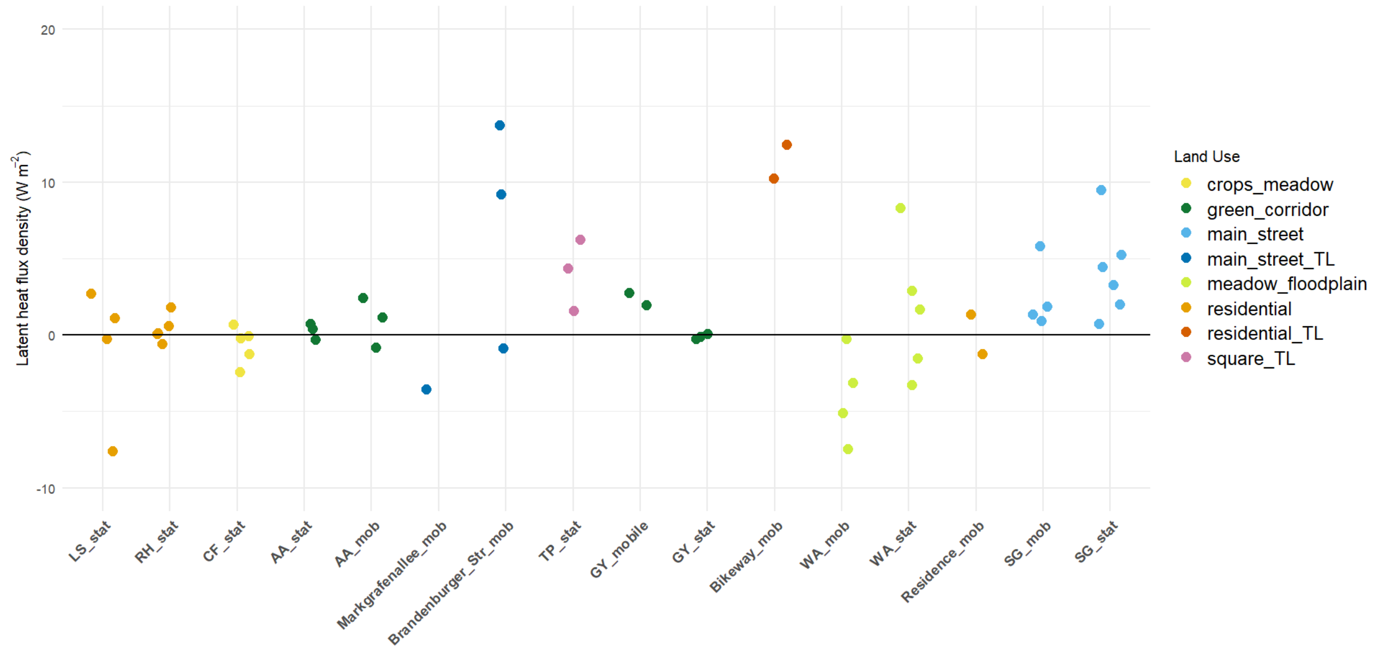

Figure 3.15 Latent heat flux densities at the 02:00 CEST measurement ride. The x-axis shows the different locations along the measurement route, marked with ‘stat’ for a stationary measurement, where the bike was parked, and with ‘mob’ for a mobile measurement during riding. The data points are colour coded according to the land use classifications shown in Figure 2.6.

At 02:00 CEST, the values of turbulent kinetic energy (TKE) remained generally low across the transects. Higher TKE values were observed at some residential locations (e.g. LS and RH), along the mobile transect at AA, and at the GY mobile measurement, where values exceeded 1 $m^2\ s^{-2}$. Elevated values also appeared at the urban transects of St. Georgen main street. In contrast, locations in the WA floodplain, at CF and AA, and at the GY stationary site showed values close to zero, indicating weak turbulence (Figure 3.16).

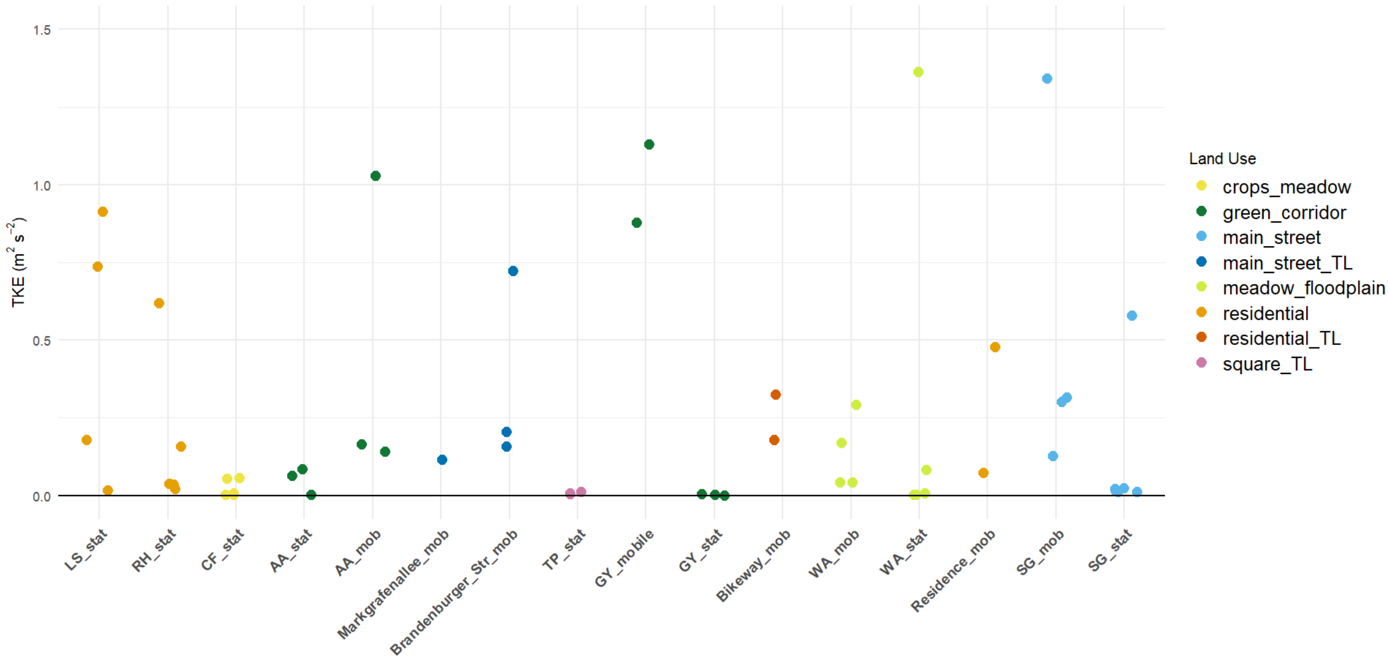

Figure 3.16 Turbulent kinetic energy at the 02:00 CEST measurement ride. The x-axis shows the different locations along the measurement route, marked with 'stat' for a stationary measurement, where the bike was parked, and with 'mob' for a mobile measurement, recorded while riding. The data points are colour coded according to the land use classifications shown in Figure 2.6.

The CO_2 flux density exhibited a wider range of values, particularly at the Wilhelminenaue floodplain, where values ranged from –20 µmol $m^{-2}\ s^{-1}$ at the stationary site to +20 µmol $m^{-2}\ s^{-1}$ during the mobile transect. Elevated values were also recorded along the bikeway transect. The GY mobile transect showed fluxes similar to those at the WA stationary site. At most other locations, fluxes remained close to zero. In contrast, the more urban parts of Brandenburger Straße, Tekirdagplatz, and St. Georgen main street consistently showed positive values, whereas in the residential areas, as well as at CF and AA, fluxes fluctuated around zero.

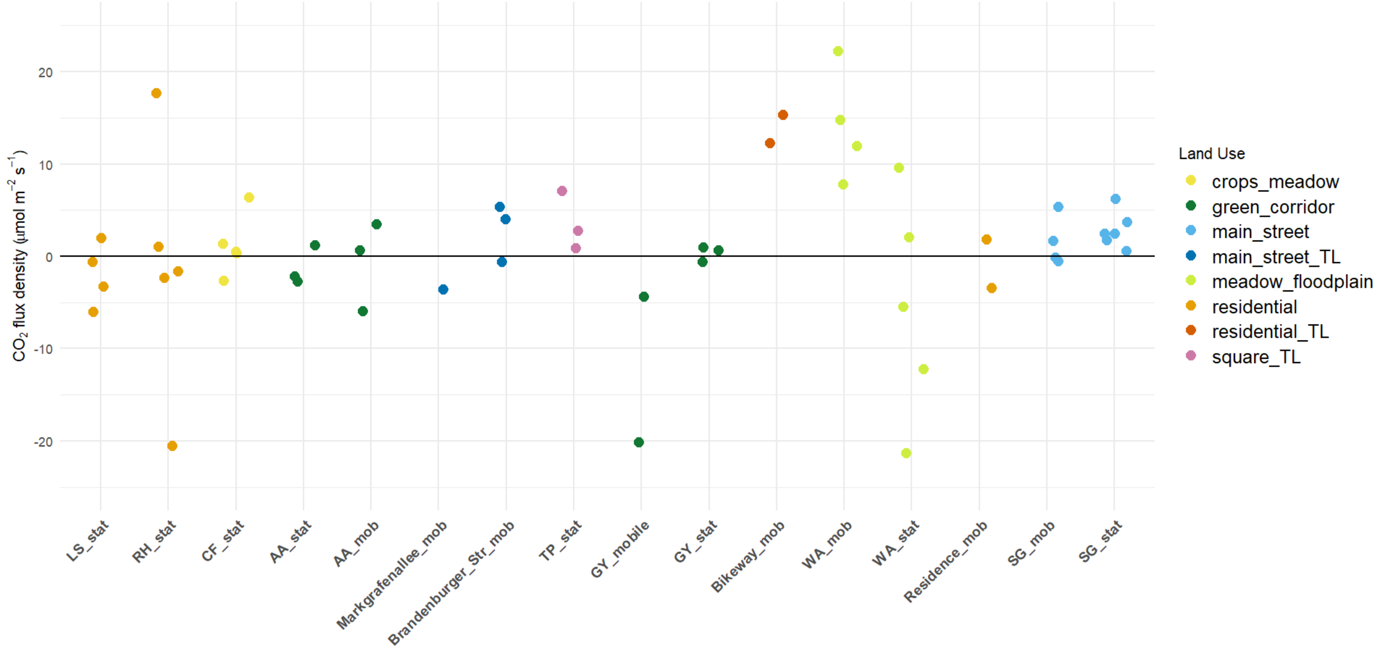

Figure 3.17 CO_2 flux densities at the 02:00 CEST measurement ride. The x-axis shows the different locations along the measurement route, marked with 'stat' for a stationary measurement, where the bike was parked, and with 'mob' for a mobile measurement, recorded while riding. The data points are colour coded according to the land use classifications shown in Figure 2.6.

The fluxes of the 00:00 CEST measurement ride are provided in the appendix (Figure A. 18, A. 19, A. 20, A. 21).

4. Discussion

In the discussion, the hypotheses formulated are examined on the basis of the available results. The extent to which the hypotheses can be refuted is discussed. The results are compared, and sources of uncertainty are examined.

4.1 Urban heat island in St. Georgen/Burg

In this thesis MWS data and the results of mobile measurements were combined to investigate the microclimate conditions in more detail in the St. Georgen/Burg district during summer. The MWS data enabled spatially continuous monitoring, while mobile measurements provided a more detailed overview of the selected area. Based on the morphological characteristics of the surroundings of the MWS along the route, land use classes were defined to differentiate the intensity of the UHI.

One objective was to quantify the UHI effect during summer nights in the St. Georgen/Burg district and investigate its spatial and temporal manifestation as well as different nightly synoptic situations.

The measurements demonstrate pronounced nocturnal urban–rural contrasts in the St. Georgen/Burg district, with UHI magnitudes up to 5 K and a peak around 21:00 CEST. This magnitude and timing are consistent with classical UHI mechanisms: urban materials with low albedo and high heat capacity store daytime radiation induced heat and release it during the night, producing sustained sensible heat fluxes. The results show a distinct connection between UHI intensity and building density and vegetation. The urban stations were consistently warmer, with SG exhibiting the largest temperature difference relative to the rural reference station EBG. The cconditions given there, high surface sealing, reduced ventilation, increase nocturnal heat retention and delay radiative cooling. The semi-urban stations were in average still warmer than the EBG, yet approximately 2 K cooler than the urban sites, indicating that openness and vegetation reduce heat retention and allow faster cooling.

Comparing these results to other studies on the UHI, which have shown its variability among different city sizes, climates and latitudes, Oke (1973) estimated an UHI magnitude of 4-5 K for European cities with a population of around 100,000 inhabitants. Also Spies (2019) showed an average UHI of 4.8 K during the night of extreme days in the Bayreuth city center. The results of this thesis align with these but also nuance the urban/semi-urban dichotomy: cooling and nocturnal persistence depend more strongly on specific site morphology (tree cover, sky-view factor, canyon aspect, imperviousness) than on simple land-use labels.

Even when considering all cold-air nights, not only those under autochthonous synoptic conditions, the UHI effect remained evident. This indicates that urban sites experience significantly reduced cooling efficiency compared to rural reference conditions, especially under radiative cooling scenarios. This persistence of the UHI under favourable cooling conditions highlights its implications for urban heat stress and nighttime thermal comfort. The results point to a significant difference in UHI between the urban and semi-urban stations, underlining the cooling effectiveness of open space and vegetation.

With three tropical nights Bayreuth lies within the national average of Germany (Deutscher Wetterdienst, 2025a). Despite the common classification as tropical nights according to the DWD criterion, the individual nights showed substantial differences in their thermal evolution and spatial distribution within the MWS and within each other.

The tropical night on July 21st fulfilled the cold air criteria in 12% of the observations, presumably due to cloud cover and generally warm synoptic conditions in the whole city. The constant temperatures close to the threshold indicate a balance between radiative cooling and synoptic forcing, while the slight evening warming suggests advection of warmer air or reduced ventilation. The stronger cooling at the GY and AA stations indicates effective local cooling in areas with higher vegetation and lower building density. The drop of nearly all stations below the 20 °C threshold in the morning suggests turbulent mixing after the morning transition, mixing in cold air from the rural surroundings.

On August 14th, with the cold air criteria fulfilled to 36%, the more continuous cooling points to more stable atmospheric conditions with limited synoptic disturbances. Only four stations fulfilled the tropical night definition, underlining the spatial heterogeneity of the UHI. Particularly, LS and RH only barely remained above the threshold, and their brief drop below 20 °C at 07:00 CEST emphasizes the sensitivity of classification to short-term cooling phases. The larger temperature offset between GY/AA and the remaining network illustrates their persistent role as local cold spots, especially under calmer meteorological conditions.

August 24th (44% fulfilled cold air criteria) stands out due to the atypical course with a cooling phase until 01:00 CEST, followed by a short warming, and subsequently a rapid temperature decline in the morning hours. This indicates the passage of a synoptic disturbance, likely associated with frontal activity.

Across all three events, the spatial variability within the MWS remained limited, as differences between the coldest (GY, AA) and the warmest stations did not exceed 1-2 K. This narrow distribution suggests that during synoptic control, local effects of vegetation, building density, or cold-air drainage play a secondary role compared to large-scale atmospheric dynamics. Nevertheless, the consistent lower temperatures of GY and AA, relative to the threshold, underlines the resilience of vegetated and agricultural land uses in mitigating extreme nocturnal heat.

In conclusion, and in line with the classification of Bayreuth into warm and cold areas by Tschuschke (2019), the St. Georgen/Burg district can be regarded as part of the warmer areas of the city of Bayreuth, while local cold islands (GY, AA) exist but do not provide effective cooling for the district.

The results partly support the hypothesis that UHI intensity is greatest in densely built, poorly vegetated areas under calm, clear conditions. Indeed, the strongest contrasts occurred at urban sites such as SG. However, the limited spatial variability during synoptic influence and the persistence of higher temperatures at some semi-urban sites highlight that building density and vegetation alone cannot explain UHI intensity. Instead, factors such as canyon geometry, station orientation, and ventilation pathways also play a decisive role.

4.2 Early morning transition

The analysis of morning warming rates revealed clear differences between stations, indicating that a simple classification into urban, semi-urban, and rural categories is insufficient to explain early-morning temperature dynamics. To capture spatial patterns more accurately, additional variables need to be considered. Two semi-urban stations (GY and CF) exhibited the highest heating rates after sunrise. This is consistent with the expectation that locations with more open space warm more rapidly due to earlier exposure to solar radiation. However, this pattern was not observed at AA and BG, where tree cover likely delayed warming despite similar land-use characteristics. Conversely, urban stations with open space warmed up faster (LS, SG), while the latest maximum heating rate occurred at RH, suggesting prolonged shading. Additionally, accounting for station orientation, LS and SG show an eastward exposure, which likely accelerates their morning warming. This orientation allows earlier direct solar radiation after sunrise compared to the other urban sites, thereby supporting the observed faster increase in air temperature. In contrast, TP and RH are shaded by adjacent buildings on their eastern side, which delays direct solar exposure after sunrise and likely accounts for their slower morning warming.

These findings highlight the influence of local site characteristics – particularly shading, vegetation cover, orientation and sky view – on morning temperature evolution. Although previous studies (Oke et al., 2017; Stewart et al., 2014) emphasize the distinction between urban and rural environments, the results indicate that for warming rates, a more fine-grained analysis of micro-scale features is necessary. The results are consistent with Sungur et al. (2025), whose method formed the differentiation of the stations. They demonstrated that urban/semi-urban/rural classifications provide a robust framework for describing average diurnal temperature cycles. However, this approach fails to adequately capture short-term processes such as morning warming rates. Taken together, both studies highlight that while broad categorizations are useful for general climatological assessments, a more detailed consideration of micro-scale morphology and exposure conditions is essential for understanding temperature dynamics during the early transition period.

Locations that experienced stronger nocturnal cooling tended to warm more rapidly in the morning. This dynamic may influence UHI development, as the intensity of the UHI effect remained relatively low in the early morning but increased later in the day, reflecting the delayed warming of shaded, densely built stations. Delayed morning warming leads to a delayed and potentially dampened UHI development. This lag, observed at approximately 1–2 hours between the earliest maximum (GY at 08:00 CEST) and the latest maximum (RH at 10:10 CEST), aligns with descriptions by Oke et al. (2017) and illustrates how microclimatic differences contribute to diurnal heat distribution in urban environments.

The findings partly support the hypothesis that rural and semi-urban sites warm more rapidly after sunrise due to greater exposure to solar radiation. Indeed, GY and CF, both semi-urban and more open, exhibited the strongest warming rates. However, the absence of this pattern at AA and BG demonstrates that tree cover and shading can override land-use effects. Similarly, some urban stations (LS, SG) showed rapid warming when their orientation enabled early solar exposure, while others (TP, RH) remained delayed due to shading by adjacent buildings. These deviations highlight that land use alone cannot fully explain morning warming rates; instead, micro-scale factors such as vegetation, sky view, and station orientation critically shape early-morning temperature dynamics.

4.3 Cold air influence in St. Georgen/Burg

In general, the urban locations with higher surface sealing and building density recorded higher air temperatures compared to the more vegetated sites along the measurement route. During the 00:00 CEST ride, all urban stations exhibited higher air temperatures than more vegetated sites, reflecting the typical retention of heat in densely built environments. During the 02:00 CEST ride urban locations still exhibited higher temperatures than the vegetated sites. However, a pronounced persistence of elevated temperatures was only observed in the St. Georgen main street, while other urban areas showed a more effective cooling. This suggests that densely built street canyons with high thermal storage capacity and limited vegetation delay nighttime cooling compared to more open urban structures. The coldest areas during the night were consistently observed at the agricultural fields and gardens between and around CF and AA, as well as at the meadow and bike path near GY and the WA floodplain. But even if most of them are located within the urban district none of the colder areas appear to exert a cooling influence on their urban surroundings. Although the colder stations indicate local cold-air accumulation, no evidence of a subsequent flow into the urban core was observed.

The distribution of vapor pressure along the route further supports the importance of vegetation and local microclimatic processes. During the first ride (00:00 CEST), the highest values occurred around AA, GY, and WA, consistent with evapotranspiration in vegetated environments. At 02:00 CEST, the maxima shifted to the area between CF and AA and to several residential zones. The WA floodplain however exhibited relatively low vapor pressure values despite its vegetation, which may be explained by near-saturation conditions and associated limitations of the relative humidity leading to condensation. By 04:00 CEST, vapor pressure maxima were found in densely built urban streets, where reduced ventilation and higher air temperatures likely favored water vapor retention, while lower values occurred in the colder areas around CF and AA, pointing to cold-air pooling and reduced humidity capacity of cooler air masses.

Following the temperature distribution, it is possible, that cold air builds up at the CF and flows along the topography down to the AA. Cooling of the residential area close there is possible, low wind speeds at the base of the hill below CF indicates cold air accumulation and the wind direction along the measured route next to it points in the direction of the urban core.

The strong temperature difference also shows the cold air accumulation in the Wilhelminenaue floodplain, a process that has been documented in previous studies (Thomas et al., 2021; Tschuschke, 2019). This interpretation is further supported by the vapor pressure and relative humidity data, which indicate near-saturation conditions resulting from low temperatures in combination with high water availability.

The wind measurements complement this picture: low wind speeds are consistent with cold-air pooling, while the wind direction reveals the flow pathways of the cold air. Along the upper path, reduced wind speeds with flow aligned to the valley toward the city were observed, whereas on the lower path the flow follows the topography toward the water body. Notably, even at the slightly elevated WA station, temperatures remained comparably low, underlining the magnitude and spatial extent of cold-air accumulation in this area.

The results largely confirm the hypothesis: during the cold-air night, rural and vegetated sites (CF, AA, GY, WA) consistently exhibited lower temperatures than urban areas, and near-saturation humidity in the floodplain supports the role of cold-air pooling. The wind and vapor pressure patterns further indicate drainage along topography and accumulation in depressions, consistent with expected cold-air dynamics. However, no evidence was found that these colder air masses penetrated into the urban core, suggesting that while pooling and drainage occur locally, their cooling influence remains spatially confined.

4.4 Flux densities during a cold air night

The interpretation of the measured fluxes involves a degree of uncertainty, as nighttime turbulent fluxes are naturally low and the short perturbation time applied in this study introduces systematic underestimation, while random variability further increases scatter. Nevertheless, the spatial patterns and relative differences observed across sites likely reflect true signals, even if absolute flux magnitudes should be interpreted with caution. Measurement uncertainties will be discussed in detail in chapter 4.5. Consequently, the focus of this section is placed on identifying spatial patterns in the fluxes rather than on their absolute magnitudes.

The sensible heat flux measurements reveal a distinction between different land use types. Maximum values were observed in areas with high building density and surface sealing, while vegetated sites, such as the Wilhelminenaue floodplain and gardens, exhibited near zero and negative fluxes, indicating surface cooling and energy loss to the atmosphere. Overall, nighttime fluxes were low across all transects, which is consistent with the general reduction in turbulence and energy exchange during stable nocturnal stratification.

These results do not completely align with previous studies, such as Yap & Oke (1974), who reported exclusively upward sensible heat fluxes during the night in Vancouver at 1.2 m measurement height, emphasizing the role of stored heat release from urban surfaces as a source term in UHI development. The contrast between sealed and vegetated surfaces in this study similarly highlights the importance of surface properties in modulating nocturnal energy fluxes. Schmid et al. (1991) also documented pronounced differences in flux densities between nearby sites with varying land cover, further underlining the strong spatial heterogeneity of surface-atmosphere interactions in urban environments. While the absolute flux values are low, the observed spatial variability demonstrates that surface sealing and morphology influence nighttime energy distribution and contribute to persistent urban-rural temperature gradients.

The latent heat flux measurements at 02:00 CEST exhibit a pronounced spatial variability. The highest positive fluxes were observed in densely built urban areas, suggesting evapotranspiration processes in areas where the enthalpy associated with longwave radiation storage in urban structures sustains higher surface temperatures overnight. In contrast, negative fluxes occurred primarily at the Wilhelminenaue floodplain, likely indicating surface condensation under stable, moisture-rich conditions. The wider range of flux values recorded at this site reflects the dynamic interplay of cold-air accumulation, radiative cooling, and local moisture availability. Measurements under tree lines also showed elevated fluxes, which may result from enthalpy storage within the canopy layer, leading to localized warming and increased latent heat exchange. Most other transects, particularly in open residential and agricultural areas, were near zero, which aligns with the expected suppression of evapotranspiration and turbulent fluxes during nighttime stability. These findings underscore the influence of building geometry on nocturnal latent heat flux patterns, supporting observations by Zhu et al. (2024), who demonstrated that stored heat, created by longwave radiation during the day, in dense urban areas can sustain heat fluxes overnight, thereby contributing to the persistence of the UHI effect.

A comparison of TKE values between the rides at 00:00 CEST and 02:00 CEST indicates a general decrease in turbulence intensity during the night, reflecting the expected stabilization of the nocturnal boundary layer. However, some locations still exhibit comparatively elevated TKE values, which is notable given the typically low nocturnal turbulence levels. These local maxima likely point to persistent mechanical turbulence generated by urban roughness elements, such as building geometry and street canyons. This highlights that even under predominantly stable nighttime conditions, urban form and terrain can sustain small-scale turbulence which may influence local heat and moisture transport.

The CO_2 flux measurements reveal spatial variability, with the Wilhelminenaue floodplain standing out due to its wide range of values (–20 µmol m^{-2} s^{-1} at the stationary site to positive fluxes of similar magnitude during the mobile transect). At night, photosynthetic uptake ceases, and vegetation acts primarily as a CO_2 source through respiration. Negative fluxes in the floodplain likely reflect cold-air pooling, which traps respired CO_2 close to the surface and leads to intermittent downward fluxes, while positive values during the transects suggest localized mixing events that released accumulated CO_2 into the atmosphere. These contrasting signals highlight the sensitivity of nocturnal CO_2 exchange to the interplay between vegetation respiration, boundary-layer stability, and small-scale drainage dynamics. Overall, the measured CO_2 fluxes appear relatively high compared to findings by Vesala et al. (2008), though their measurements were conducted at 31 m above ground level, where turbulent mixing would dampen surface exchange signals, suggesting that the differences are at least partly attributable to the lower measurement height in this study. Positive fluxes recorded consistently in dense urban areas such as Brandenburger Straße, Tekirdagplatz, and St. Georgen main street are indicative of anthropogenic emission or in vegetated areas indicating plant respiration. Whereas near-zero or fluctuating fluxes in residential and vegetated areas point to a balance between CO_2 uptake and release.

The observed flux patterns are largely consistent with the initial hypothesis. Sensible heat fluxes in densely built urban areas were indeed higher and predominantly positive, reflecting the combined effects of anthropogenic heat release and heat storage in urban materials, while rural and vegetated sites, particularly the Wilhelminenaue floodplain, exhibited near-zero or slightly negative fluxes in line with cooling and cold-air accumulation processes. Similarly, latent heat fluxes were negative at the floodplain, suggesting condensation under stable, moisture-rich conditions, whereas positive fluxes persisted in the urban core where elevated surface temperatures maintained evapotranspirative activity. These findings support the hypothesized contrast between urban and rural land uses, while also emphasizing the role of local morphology and microclimatic dynamics in modulating nocturnal flux exchanges.

4.5 Sources of uncertainty

For the MWS, a key source of uncertainty lies in the comparability between the "old" and newly installed stations. A testing phase with all sensors operating side by side prior to deployment would have improved calibration consistency and ensured data homogeneity. Furthermore, the placement of the stations warrants careful attention, on the one hand regarding the sky view factor, which influences radiative cooling and heating patterns and can introduce bias in temperature measurements. On the other hand, the exact positioning within the land-use transect can lead to localized effects, which may not be representative of the wider land use category. Future measurement campaigns should therefore emphasize harmonized station calibration, standardized placement protocols, and explicit quantification of micro-environmental influences to ensure comparability and reproducibility.

The mobile measurements were subject to some methodological limitations that constrain the robustness of the results. The use of the SmartFlux3 system, which was originally designed for stationary operation, caused recurring errors in data logging. The system proved insufficiently robust for repeated mobile on–off operation, suggesting that future campaigns would benefit from the use of more reliable datalogger setups specifically adapted for mobile use.

Systematic underestimation of fluxes occurred due to the cutting of Ogives given by the short perturbation time, particularly relevant during nocturnal conditions when turbulent fluxes are generally low. As a result, the flux magnitudes presented here likely underestimate the true exchange rates, and interpretation should focus primarily on spatial variability rather than absolute values.

The number of valid flux data points was limited, as each transect was only crossed once. In some cases, the crossing time of a transect equaled the perturbation time, which resulted in a single data point for the entire transect. This lack of redundancy reduces statistical robustness. Future campaigns should therefore reduce driving speed or repeat transects multiple times to increase data density and reliability.

A further limitation lies in the spatial setup of the transects themselves. The chosen routes were not always fully open-spaced, as recommended for energy balance studies, but instead were also influenced by adjacent urban parameters like houses or cars. This heterogeneity complicates the assumption of steady-state conditions. Additionally, the chosen transects do not cover all land use types and are therefore not completely spatial representative.

Taken together, these factors restrict the comparability of flux magnitudes to other studies and underline the exploratory character of the mobile flux measurements presented here. They nevertheless provide valuable insight into relative spatial differences, but future campaigns should address these methodological shortcomings to improve robustness and interpretability.

5. Conclusions

In this thesis summer nighttime UHI intensity and cold-air dynamics within the St. Georgen/Burg district of Bayreuth were evaluated, with the expectation that densely built, little vegetated areas would retain more heat, while open, vegetated spaces would cool more effectively, particularly under calm, clear conditions. To quantify the magnitude of thermal contrasts and assess the influence of land use on nocturnal heat retention and cold air dynamics, a combination of stationary and mobile meteorological measurements was conducted on a street-canyon scale.

The results confirm that Bayreuth, despite its medium size, exhibits UHI magnitudes of up to 5 K, consistent with values observed in larger European cities. The intensity was most pronounced during radiative cooling nights under autochthonous synoptic conditions, highlighting the strong role of limited mixing. Within St. Georgen/Burg building density and vegetation emerged as decisive factors: urban areas experience little nocturnal cooling, while only a few localized cold spots, such as the meadow and vegetated areas around GY and AA, provide notable temperature relief. However, these cold-air reservoirs remain largely disconnected from the densely built-up district, and cold-air inflow from nearby open areas, such as the CF site, is insufficient to penetrate the urban core.

The flux measurements add an important layer to this picture: persistent nocturnal sensible and latent heat release from built-up areas confirms that stored daytime heat continues to drive UHI intensity after sunset. However, methodological limitations of the mobile EC setup restrict the interpretation of absolute magnitudes. Nevertheless, the spatial patterns observed provide valuable indications of localized flux variability tied to vegetation and urban form.

Overall, this thesis demonstrates the interplay between land use, urban form, and atmospheric dynamics in shaping nighttime thermal environments. The findings show that effective urban heat mitigation cannot rely on broad classifications alone, but must consider micro-scale morphology, vegetation integration and the connectivity of cold-air pathways. By linking stationary and mobile observations, this study provides both methodological insight and practical guidance for designing cooler, more resilient urban districts.

6. Acknowledgements

I wish to thank everyone, who supported me in completing my Bachelor thesis. First and foremost, I thank Prof. Dr. Christoph Thomas for advising and mentoring my work and for the motivation and his time for discussions and feedback. I am also grateful for the opportunity to use his self-written code *bmmflux*, which greatly facilitated the data processing.

I would like to thank Johannes Olesch and Markus Friedrich for their technical expertise and their support in setting up the MWS and designing and installing the MobiFast bike system. My thanks also go to the entire Micrometeorology group for the continuous feedback and encouragement, with special appreciation to Wolfgang Babel for his availability to answer questions and offering help.

Further thanks go to Leyla Sungur and Oliver Schappacher for offering their support and knowledge on specific topics, as well as to the “Klimaradl Bayreuth” for providing the cargo bike.

Finally, my heartfelt thanks go to Lars Spakowski for his close collaboration on this project and for his constant support, both professionally and a personally.

7. Bibliography

Arnfield, A. J. (2003). Two decades of urban climate research: A review of turbulence, exchanges of energy and water, and the urban heat island. *International Journal of Climatology*, *23*(1), 1–26. https://doi.org/10.1002/joc.859

Aubinet, M., Vesala, T., & Papale, D. (Eds). (2012). *Eddy Covariance: A Practical Guide to Measurement and Data Analysis*. Springer Netherlands. https://doi.org/10.1007/978-94-007-2351-1

Babak, O., & Deutsch, C. V. (2009). Statistical approach to inverse distance interpolation. *Stochastic Environmental Research and Risk Assessment*, *23*(5), 543–553. https://doi.org/10.1007/s00477-008-0226-6

Bayerisches Landesamt für Statistik. (2024, December 31). *Bevölkerungsstand*. https://www.statistik.bayern.de/statistik/gebiet_bevoelkerung/bevoelkerungsstand/index.html

Beckmann, S. K., Hiete, M., & Beck, C. (2021). Threshold temperatures for subjective heat stress in urban apartments—Analysing nocturnal bedroom temperatures during a heat wave in Germany. *Climate Risk Management*, *32*, 100286. https://doi.org/10.1016/j.crm.2021.100286

Deutscher Wetterdienst. (2024). *Was wir 2024 über das Extremwetter in Deutschland wissen*.

Deutscher Wetterdienst. (2025a, August). *Tropennacht*. https://www.dwd.de/DE/service/lexikon/begriffe/T/Tropennacht.html

Deutscher Wetterdienst. (2025b, September). *Wetterlagenklassifikation*. https://www.dwd.de/DE/leistungen/wetterlagenklassifikation/wetterlagenklassifikation.html?nn=16102

Feigenwinter, C., Vogt, R., & Christen, A. (2012). Eddy Covariance Measurements Over Urban Areas. In M. Aubinet, T. Vesala, & D. Papale (Eds), *Eddy Covariance* (pp. 377–397). Springer Netherlands. https://doi.org/10.1007/978-94-007-2351-1_16

Foken, T. (2007). Das Klima von Bayreuth: Status quo und Aufgaben für die Stadtplanung. *Standort*, *31*(3), 150–152. https://doi.org/10.1007/s00548-007-0045-x

Foken, T., & Mauder, M. (2024a). *Angewandte Meteorologie: Mikrometeorologische Methoden*. Springer Berlin Heidelberg. https://doi.org/10.1007/978-3-662-68333-0

Foken, T., & Mauder, M. (2024b). *Micrometeorology*. Springer International Publishing. https://doi.org/10.1007/978-3-031-47526-9

Geodaten Bayern. (2025, April). *Alkis®—Tatsaechliche Nutzung (tn)*. https://geodaten.bayern.de/opengeodata/OpenDataDetail.html?pn=tatsaechlichenutzung

Häckel, H. (2021). *Meteorologie* (9., vollständig überarbeitete und erweiterte Auflage). utb GmbH. https://doi.org/10.36198/9783838555041

Haiden, T., & Whiteman, C. D. (2005). Katabatic Flow Mechanisms on a Low-Angle Slope. *Journal of Applied Meteorology*, *44*(1), 113–126. https://doi.org/10.1175/JAM-2182.1

IPCC, Krinner, G., Mukherji, A., Thorne, P. W., Trisos, C., Romero, J., Aldunce, P., Barrett, K., Blanco, G., Cheung, W. W. L., Connors, S., Denton, F., Diongue-Niang, A., Dodman, D., Garschagen, M., Geden, O., Hayward, B., Jones, C., Jotzo, F., … Péan, C. (2023). *IPCC, 2023: Climate Change 2023: Synthesis Report. Contribution of Working Groups I, II and III to the Sixth Assessment Report of the Intergovernmental Panel on Climate Change [Core Writing Team, H. Lee and J. Romero (eds.)]. IPCC, Geneva, Switzerland.* (First). Intergovernmental Panel on Climate Change (IPCC). https://doi.org/10.59327/IPCC/AR6-9789291691647

Kaimal, J., & Finnigan, J. (1994). Atmospheric boundary layer flows: Their structure and measurement. *Oxford University Press*, 289 pp.

Klein Rosenthal, J., Kinney, P. L., & Metzger, K. B. (2014). Intra-urban vulnerability to heat-related mortality in New York City, 1997–2006. *Health & Place*, *30*, 45–60. https://doi.org/10.1016/j.healthplace.2014.07.014

Kuttler, W., & Weber, S. (2023). Characteristics and phenomena of the urban climate. *Meteorologische Zeitschrift*, *32*(1), 15–47. https://doi.org/10.1127/metz/2023/1153

LI-COR. (2025, August). *LI-7500DS*. https://www.licor.com/products/eddy-covariance/LI-7500DS

METEK. (2024). *Ultrasonic Wind Sensor uSonic-3 Cage MP*. https://metek.de/wp-content/uploads/2016/09/20240603_DataSheet_uSonic3_Cage_MP.pdf

METER. (2019). *METER ATMOS 41 Manual*. https://www.manualslib.com/manual/1995922/Meter-Atmos-41.html?page=8#manual

Moore, C. J. (1986). Frequency response corrections for eddy correlation systems. *Boundary-Layer Meteorology*, *37*(1–2), 17–35. https://doi.org/10.1007/BF00122754

Oke, T. R. (1969). *Towards a more rational understanding of the urban heat island*.

Oke, T. R. (1973). *City size and the urban heat island*.

Oke, T. R. (1987). *Boundary layer climates* (2nd ed). Methuen.

Oke, T. R., Mills, G., Christen, A., & Voogt, J. A. (2017). *Urban Climates* (1st edn). Cambridge University Press. https://doi.org/10.1017/9781139016476

SBG Systems. (2025, August). *Ellipse-D*. https://www.sbg-systems.com/de/ins/ellipse-d/

Schappacher, O. (2024). *Analyse der Ausprägung des Mikroklimas im Bayreuther Süden mithilfe von stationären und mobilen Messungen*.

Schmid, H. P., Cleugh, H. A., Grimmond, C. S. B., & Oke, T. R. (1991). Spatial variability of energy fluxes in suburban terrain. *Boundary-Layer Meteorology*, *54*(3), 249–276. https://doi.org/10.1007/BF00183956

Spakowski, L. (2025). *Quantifying the summer urban canopy layer heat island in a mid-sized central European city from noon to midnight: Effects of land use on spatial patterns and turbulent energy fluxes*.

Spies, I. (2019). *Urban climate – just warm streets and cool parks?*

Stadt Bayreuth. (2025). *Hitzeschutz-Strategie*. https://www.bayreuth.de/rathaus-buergerservice/planen-bauen/konzepte/hitzeanpassungsstrategie/

Stewart, I. D., Oke, T. R., & Krayenhoff, E. S. (2014). Evaluation of the 'local climate zone' scheme using temperature observations and model simulations. *International Journal of Climatology*, *34*(4), 1062–1080. https://doi.org/10.1002/joc.3746

Sungur, L., Babel, W., Späte, E., Schneider, J., & Thomas, C. K. (2025). Climate sensitive designs for policy makers: How LES model resolution affects accuracy in capturing urban micro-scale weather during heatwaves. *Urban Climate*, *61*, 102400. https://doi.org/10.1016/j.uclim.2025.102400

Taylor, G. (1938). *The spectrum of turbulence. Proc R Soc Lond A164(919)*, 476–490.

Thomas, C. K. (2025). *Christoph Thomas, trocknet Oberfranken aus?* [Broadcast]. https://fraenkischertalk.podigee.io/40-mikrometeorologe-klimaforscher-christoph-thomas-bayreuth-klima-duerre

Thomas, C. K., & Babel, W. (2022). *Vorlesung Einführung in die Meteorologie*.

Thomas, C. K., & Babel, W. (2023). *Geoökologisches Geländepraktikum (P2): Standortkundliche Methoden, Teil Mikrometeorologie*.

Thomas, C. K., Samimi, C., Lüers, J., Nölscher, A., & Held, A. (2021). *Schlussbericht zum Forschungsvorhaben Minderung Städtischer Klima- und OzonRisiken (MiSKOR)*. Uni Bayreuth.

Tschuschke, A. (2019). *Einfluss von Topografie, Fließgewässern und Bebauung auf die Temperaturverteilung und Luftströme im Bayreuther Becken—Analyse von fahrradgetragenen Messungen und Stationsdaten des MiSKOR-Messnetzes im Sommer 2019*.

United Nations Department of Economic and Social Affairs. (2014, July 10). *2014 revision of the World Urbanization Prospects*. https://www.un.org/en/development/desa/publications/2014-revision-world-urbanization-prospects.html

Vesala, T., Järvi, L., Launiainen, S., Sogachev, A., Rannik, Ü., Mammarella, I., Siivola, E., Keronen, P., Rinne, J., Riikonen, A., & Nikinmaa, E. (2008). Surface–atmosphere interactions over complex urban terrain in Helsinki, Finland. *Tellus B: Chemical and Physical Meteorology*, *60*(2), 188. https://doi.org/10.1111/j.1600-0889.2007.00312.x

Yap, D., & Oke, T. R. (1974). *Sensible Heat Fluxes over an Urban Area—Vancouver, B.C.*

Žgela, M., Lozuk, J., Jureša, P., Justić, K., Popović, M., Boras, M., & Herceg-Bulić, I. (2024). Urban heat load assessment in Zagreb, Croatia: A multi-scale analysis using mobile measurement and satellite imagery. *Environmental Monitoring and Assessment*, *196*(5), 410. https://doi.org/10.1007/s10661-024-12538-w

Zhu, L., Yang, J., Ouyang, X., Xu, Y., Wong, M. S., & Menenti, M. (2024). Street trees: The contribution of latent heat flux to cooling dense urban areas. *Urban Climate*, *58*, 102147. https://doi.org/10.1016/j.uclim.2024.102147

8. Appendix

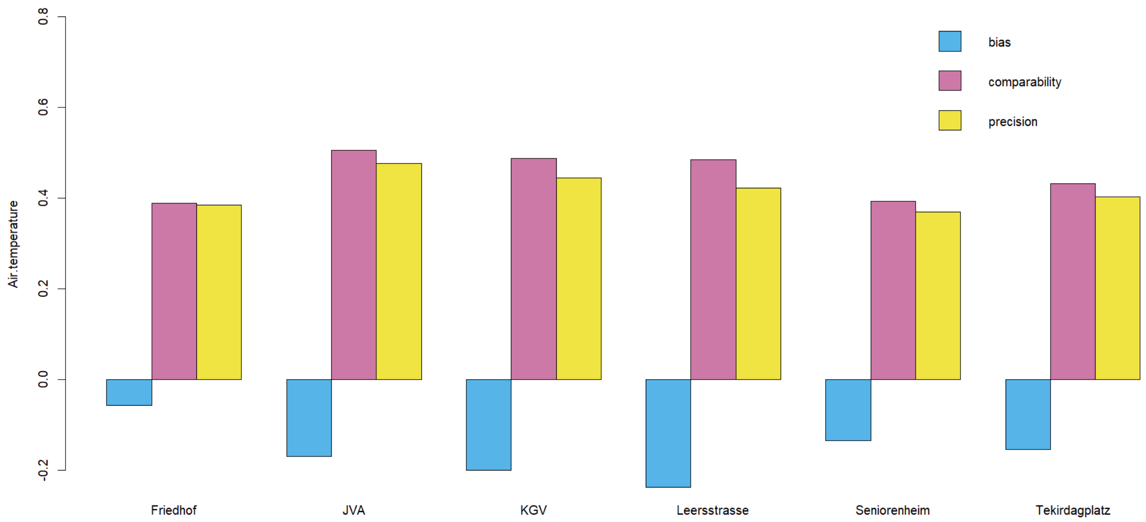

Figure A. 1 Comparability and biases of air temperature of the MWS during the test week in June 2024.

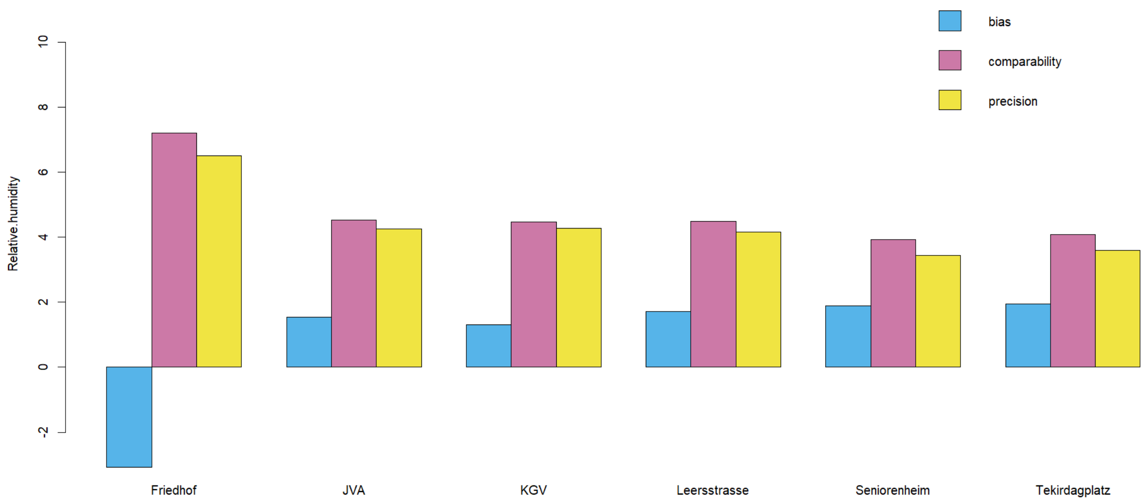

Figure A. 2 Comparability and biases of relative humidity of the MWS during the test week in June 2024.

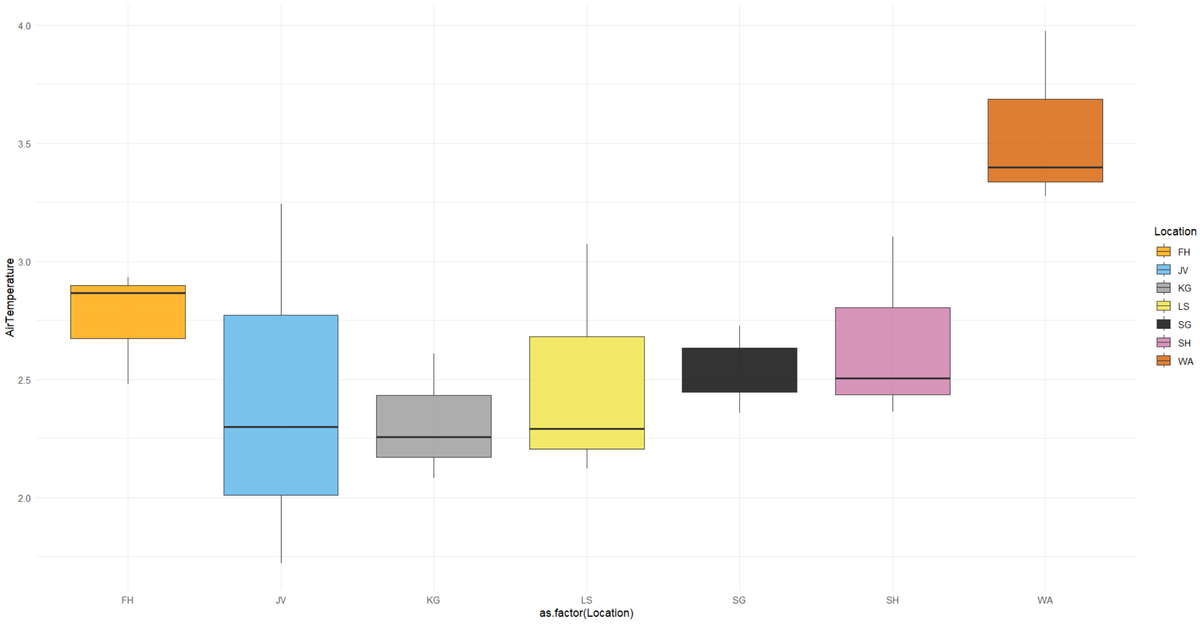

Figure A. 3 Air temperature difference between mobile and MWS measurement during the stop at the respective station.

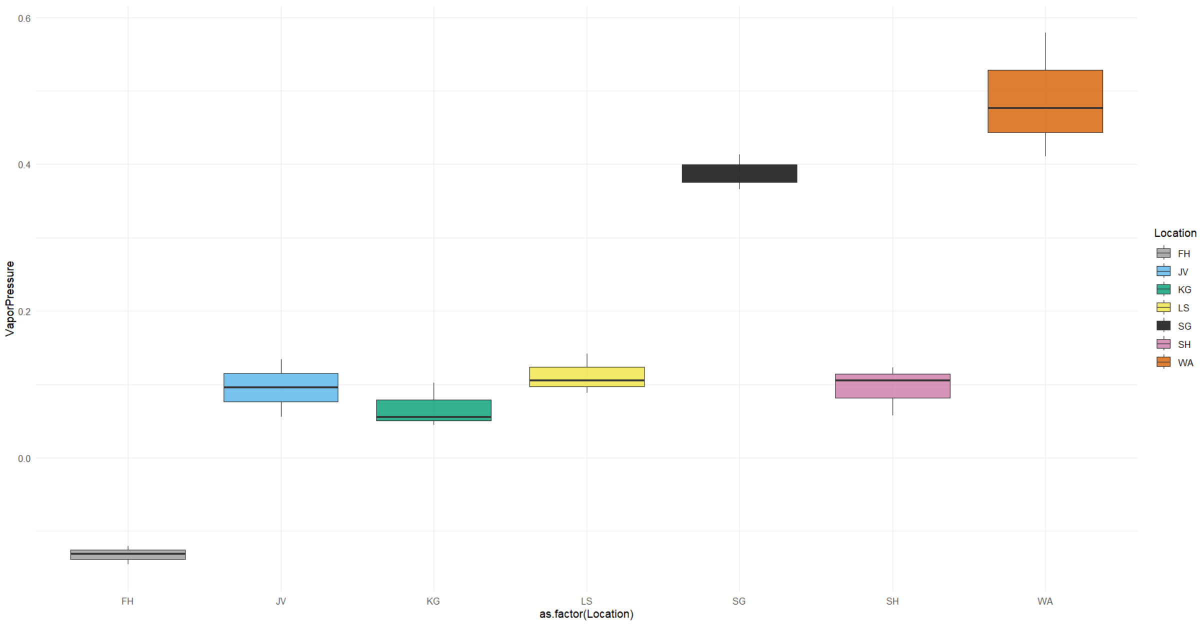

Figure A. 4 Vapor pressure difference between mobile and MWS measurement during the stop at the respective station.

Table A. 1 Weather conditions during July and August 2024 after the objective weather condition classification from DWD (Deutscher Wetterdienst, 2025b)

Day	Jul 24	Aug 24
1	20	9
2	10	20
3	20	10
4	14	20
5	4	10
6	29	6
7	14	29
8	19	19
9	29	10
10	19	10
11	19	10
12	39	6
13	39	29
14	14	29
15	9	9
16	19	9
17	19	9
18	4	29
19	9	6
20	6	9
21	29	14
22	10	9
23	19	9
24	15	29
25	5	14
26	9	14
27	29	4
28	15	29
29	5	29
30	5	9
31	9	6

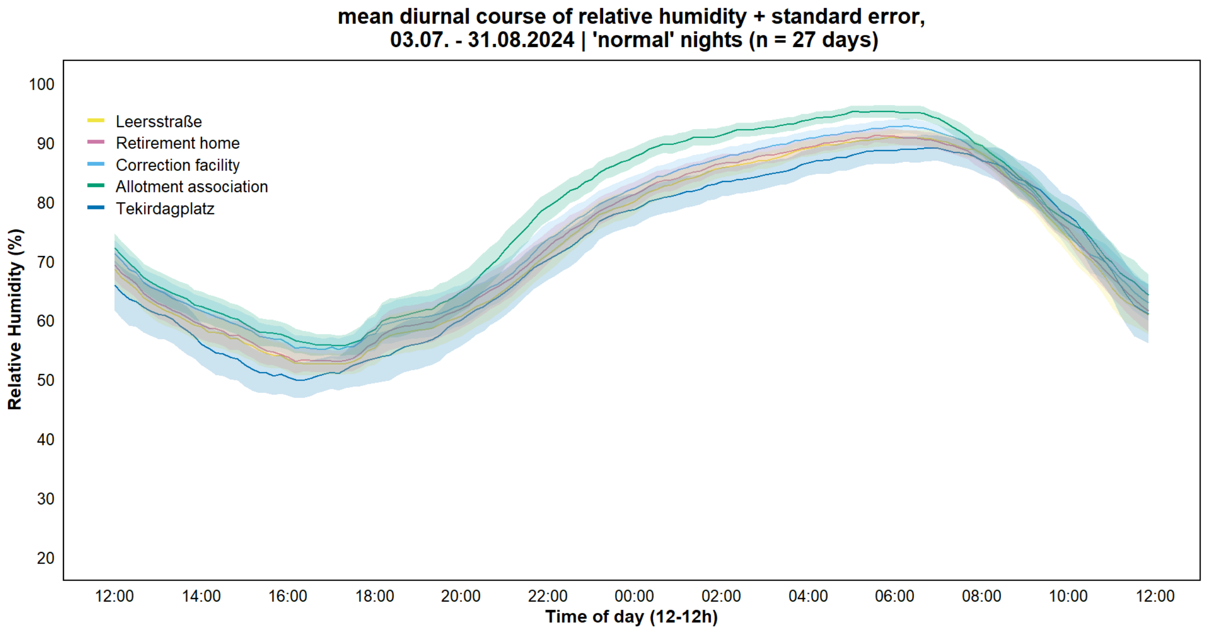

Figure A. 5 mean diurnal course of the relative humidity at the five new set up MWS with standard error during non-cold air nights (n=27) within the measurement period. (TP only August).

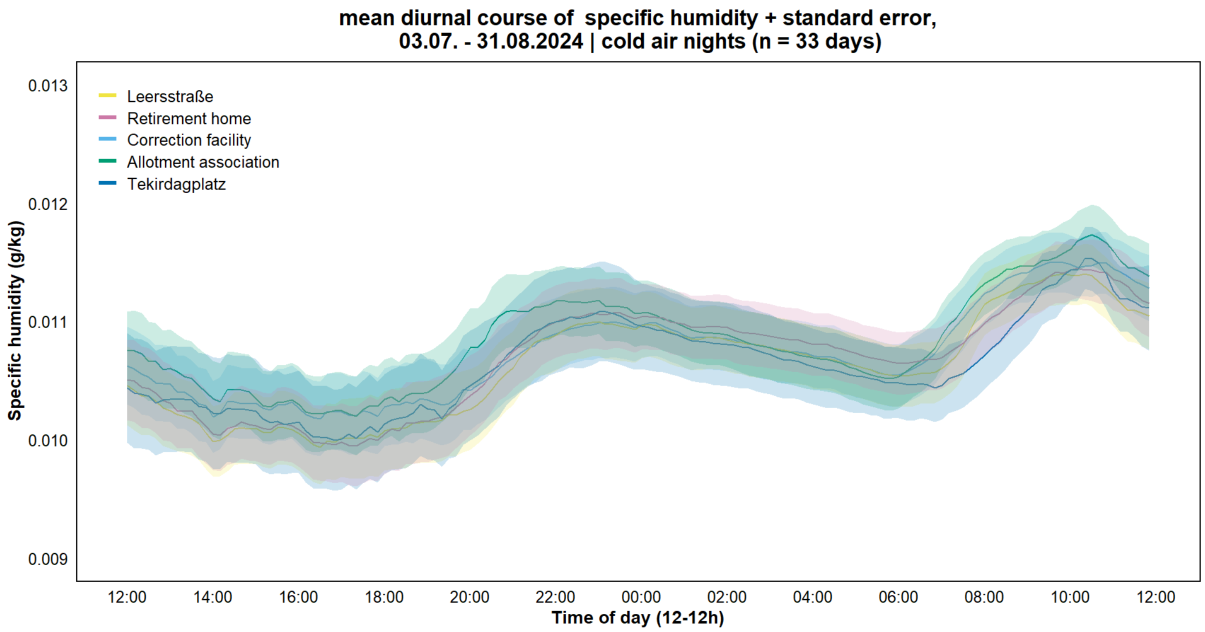

Figure A. 6 mean diurnal course of the specific humidity at the five new set up MWS with standard error during cold air nights (n=33) within the measurement period. (TP only August).

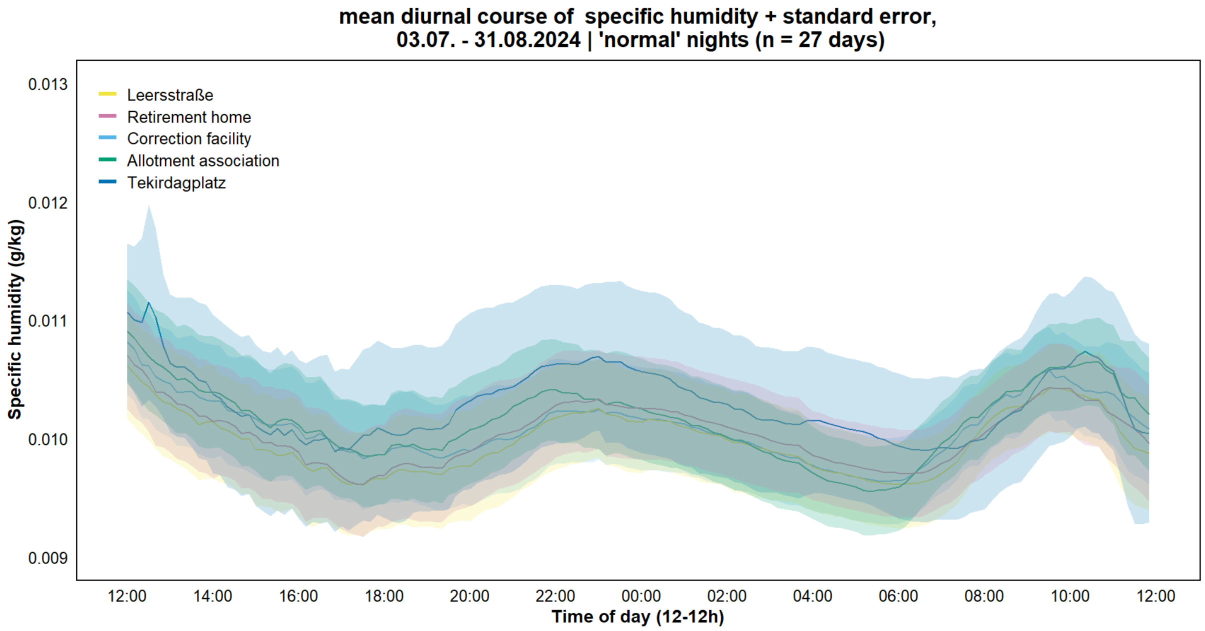

Figure A. 7 mean diurnal course of the specific humidity at the five new set up MWS with standard error during non cold air nights (n=27) within the measurement period. (TP only August).

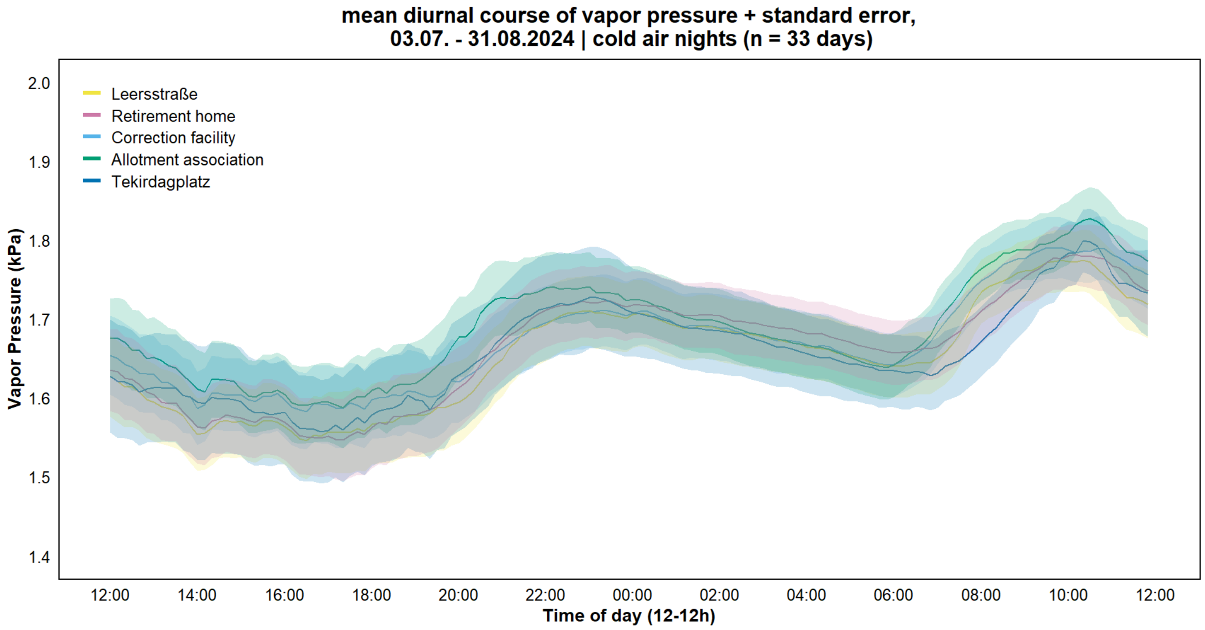

Figure A. 8 mean diurnal course of vapor pressure at the five new set up MWS with standard error during cold air nights (n=33) within the measurement period. (TP only August).

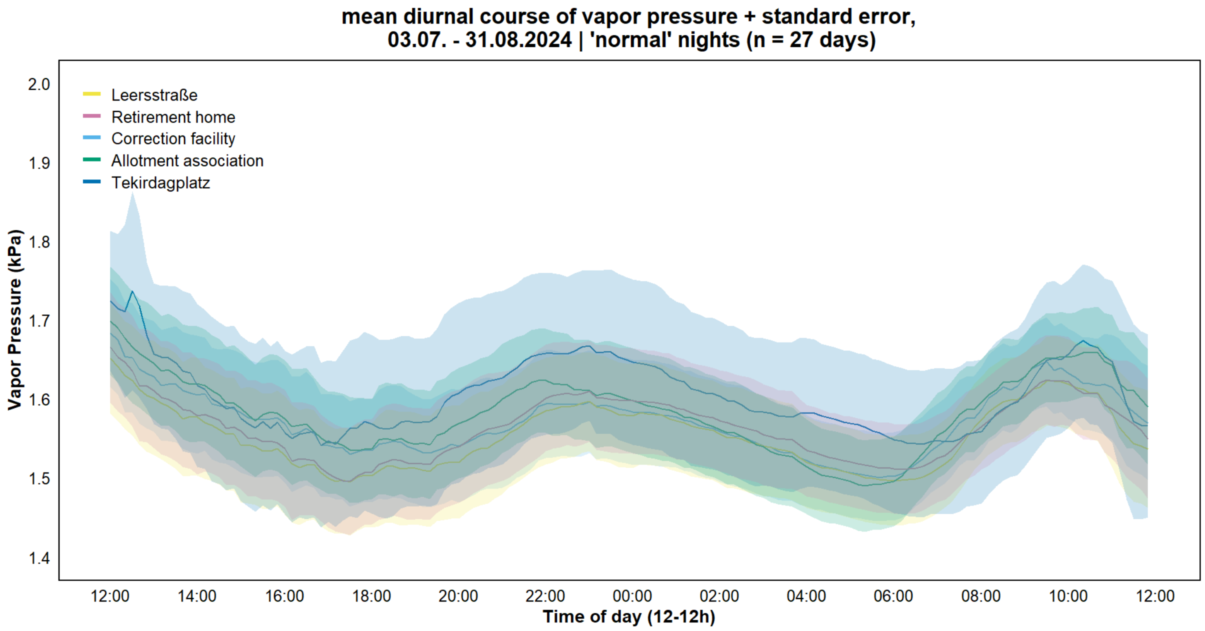

Figure A. 9 mean diurnal course of vapor pressure at the five new set up MWS with standard error during non cold air nights (n=27) within the measurement period. (TP only August).

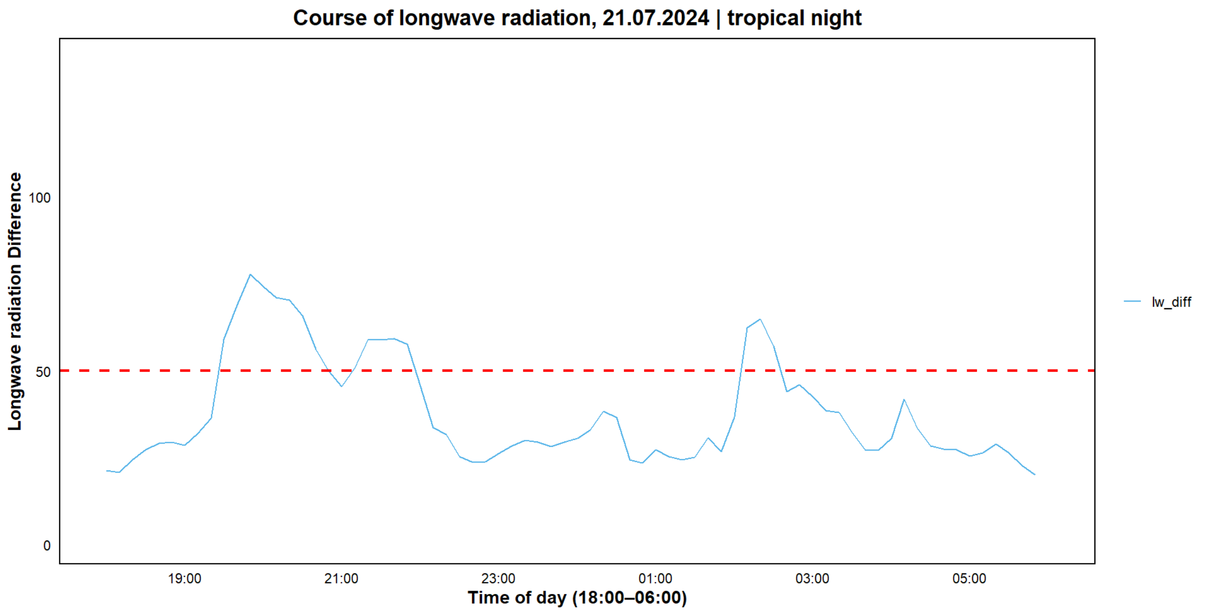

Figure A. 10 course of net longwave radiation at EBG during the tropical night on July 21st. Difference is the outgoing upward minus the incoming downward longwave radiation. The threshold marked at 50 W m^{-2} is the one determined for clear conditions in chapter 2.1.1.

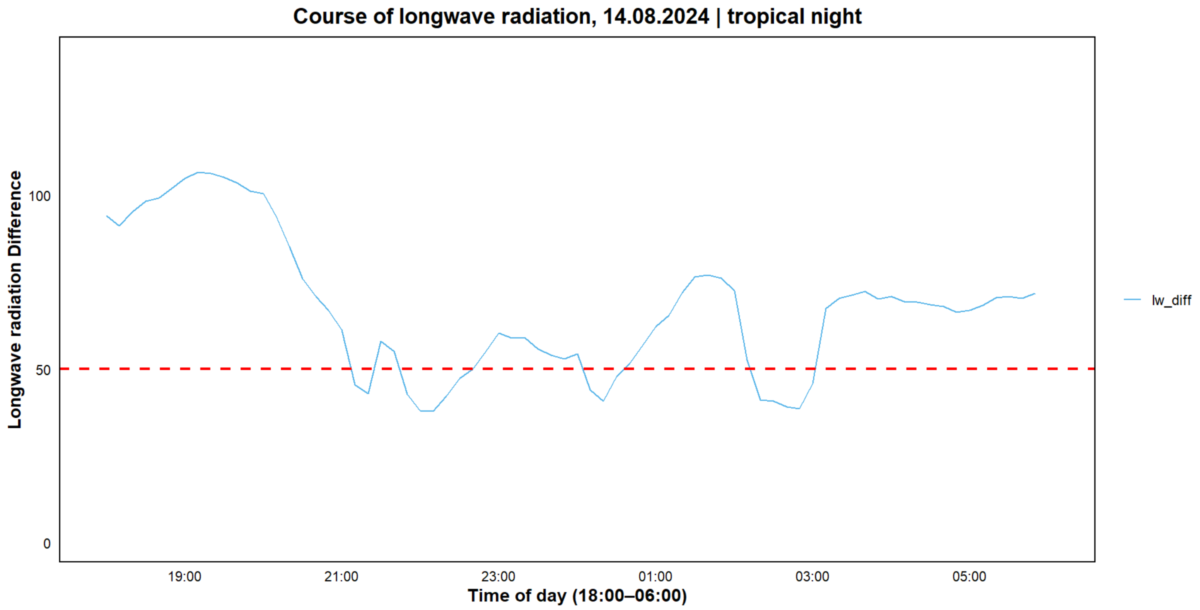

Figure A. 11 course of net longwave radiation at EBG during the tropical night on August 14th. Difference is the outgoing upward minus the incoming downward longwave radiation. The threshold marked at 50 W m^{-2} is the one determined for clear conditions in chapter 2.1.1.

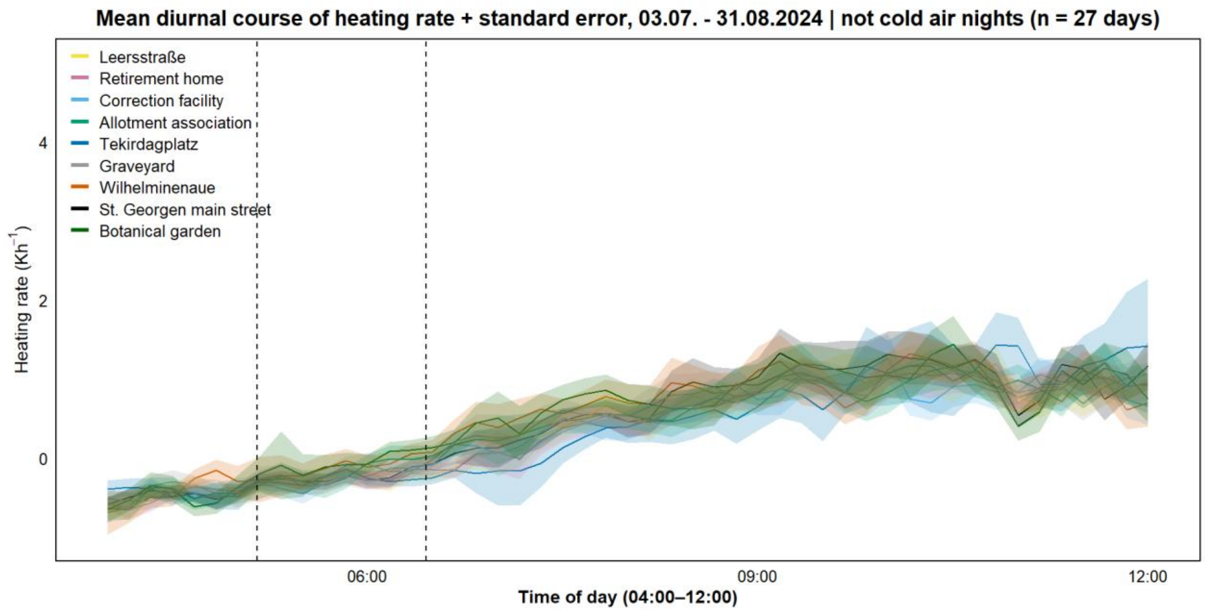

Figure A. 12 Mean diurnal course of the morning heating rate of all stations between 04:00 and 12:00 CEST with standard error after the 27 non cold air nights. The dashed lines show the time frame of the sunrise during the research period.

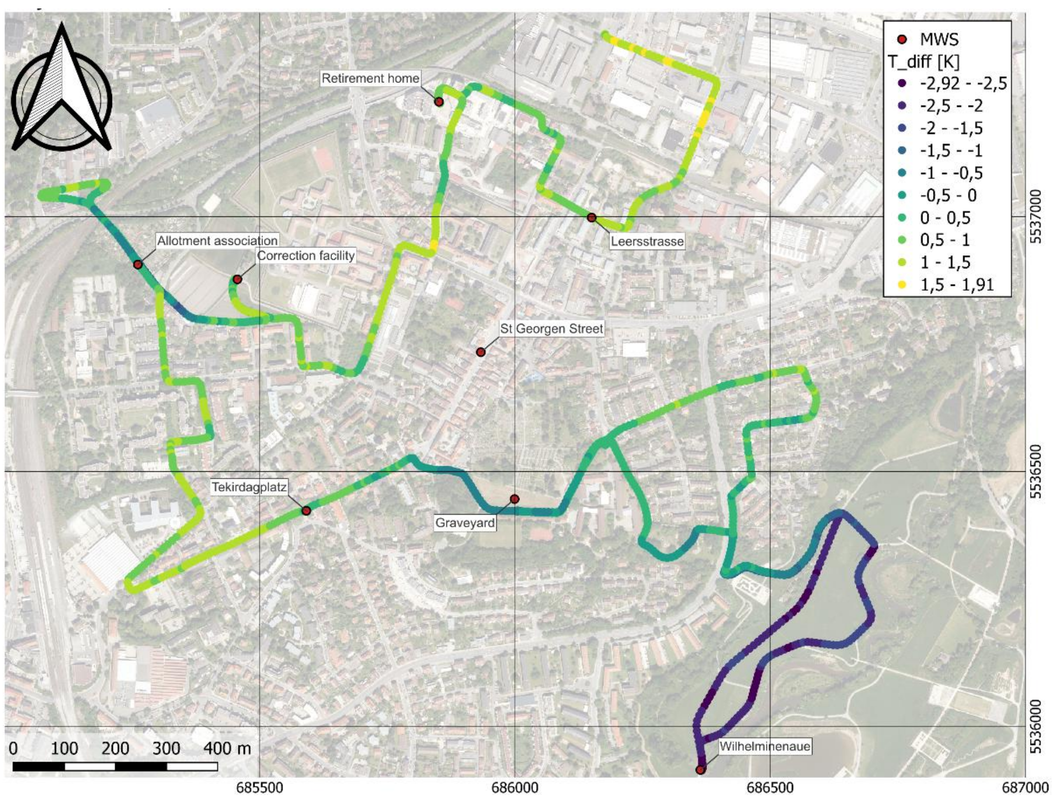

Figure A. 13 Deviation from mean corrected air temperature during the ride 00:00 – 00:59 CEST, detrended to 00:30 CEST; projection: ETRS89 / UTM zone 32N

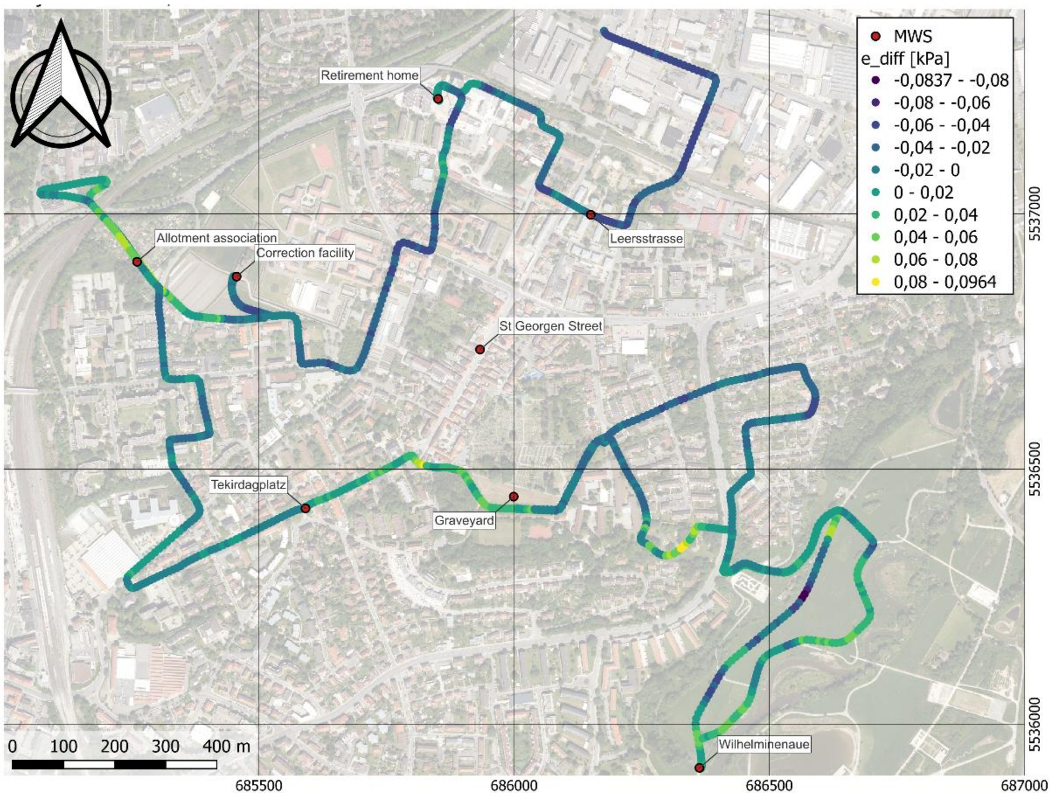

Figure A. 14 Deviation from mean vapor pressure during the ride 00:00 – 00:59 CEST, detrended to 00:30 CEST; projection: ETRS89 / UTM zone 32N

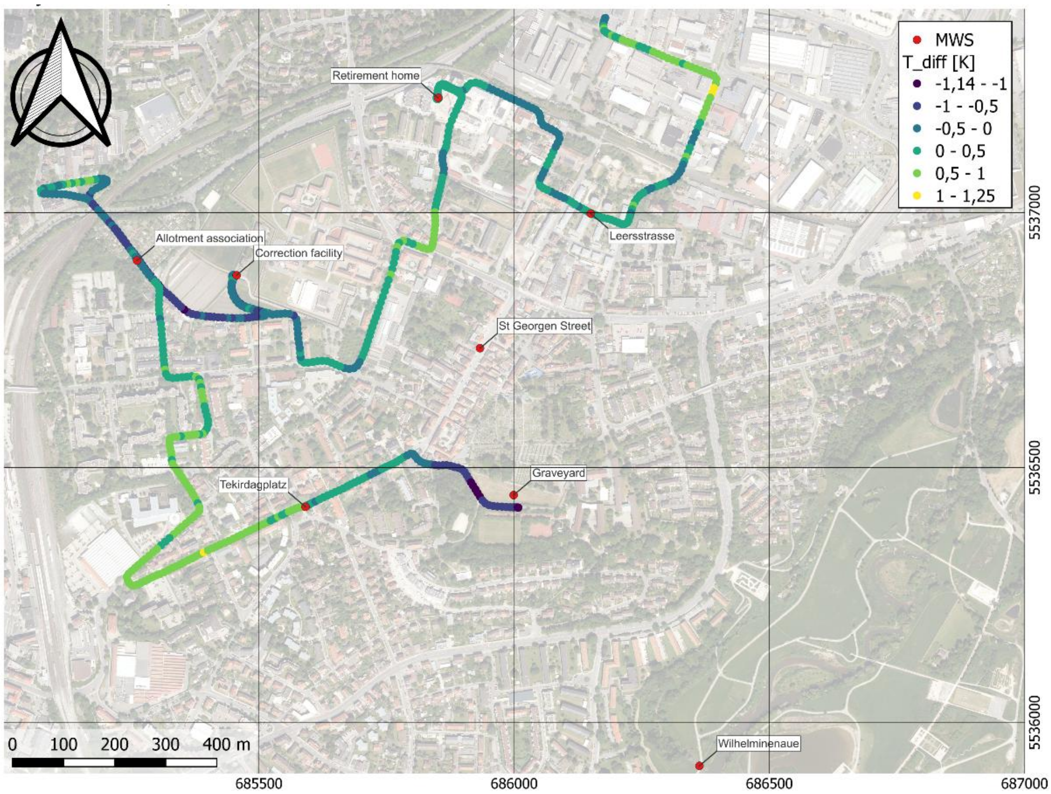

Figure A. 15 Deviation from mean corrected air temperature during the ride 04:24 – 04:59 CEST, detrended to 04:35 CEST; projection: ETRS89 / UTM zone 32N

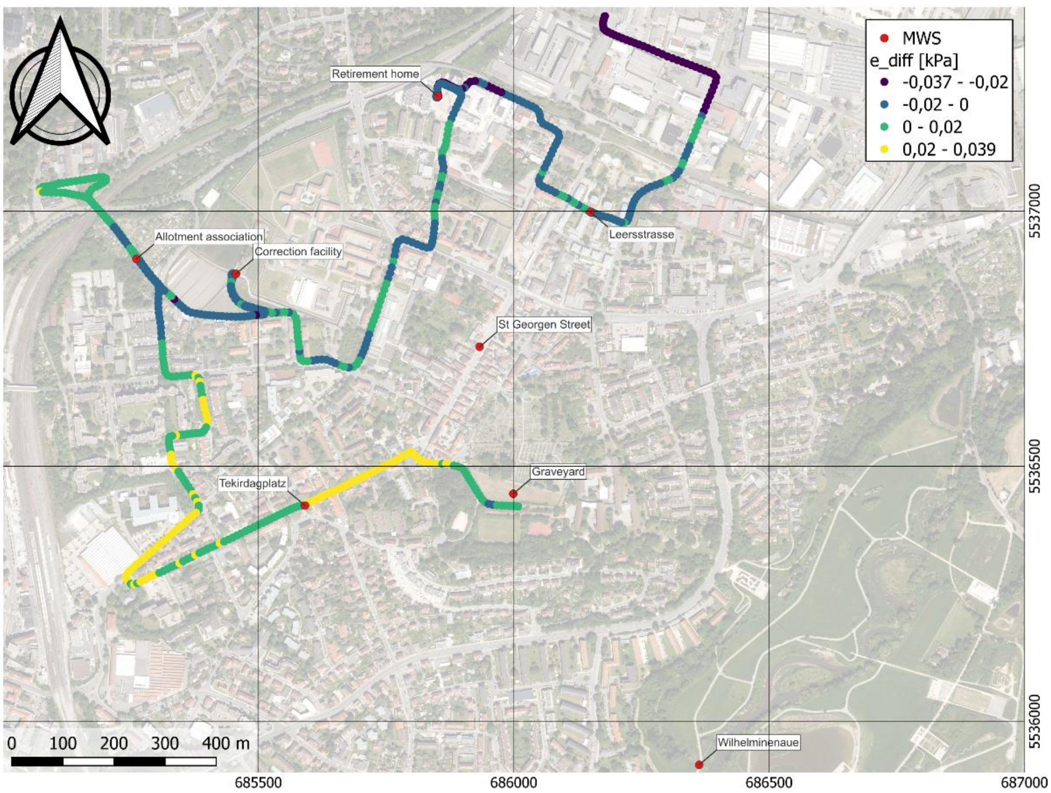

Figure A. 16 Deviation from mean vapor pressure during the ride 04:24 – 04:59 CEST, detrended to 04:35 CEST; projection: ETRS89 / UTM zone 32N

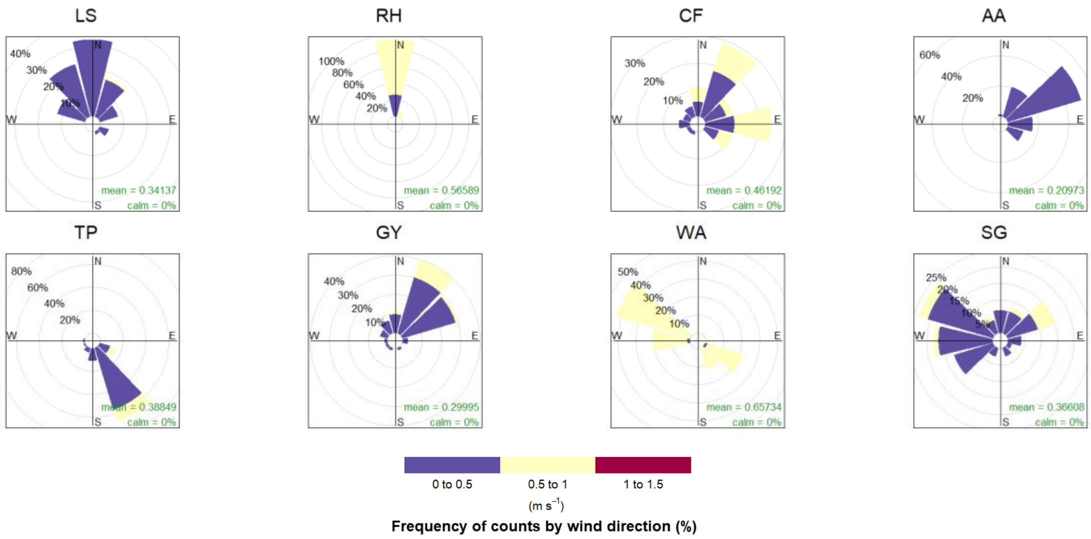

Figure A. 17 wind roses of all MWS during the night of the measurement ride August 06th, from 00:00 to 06:00 CEST

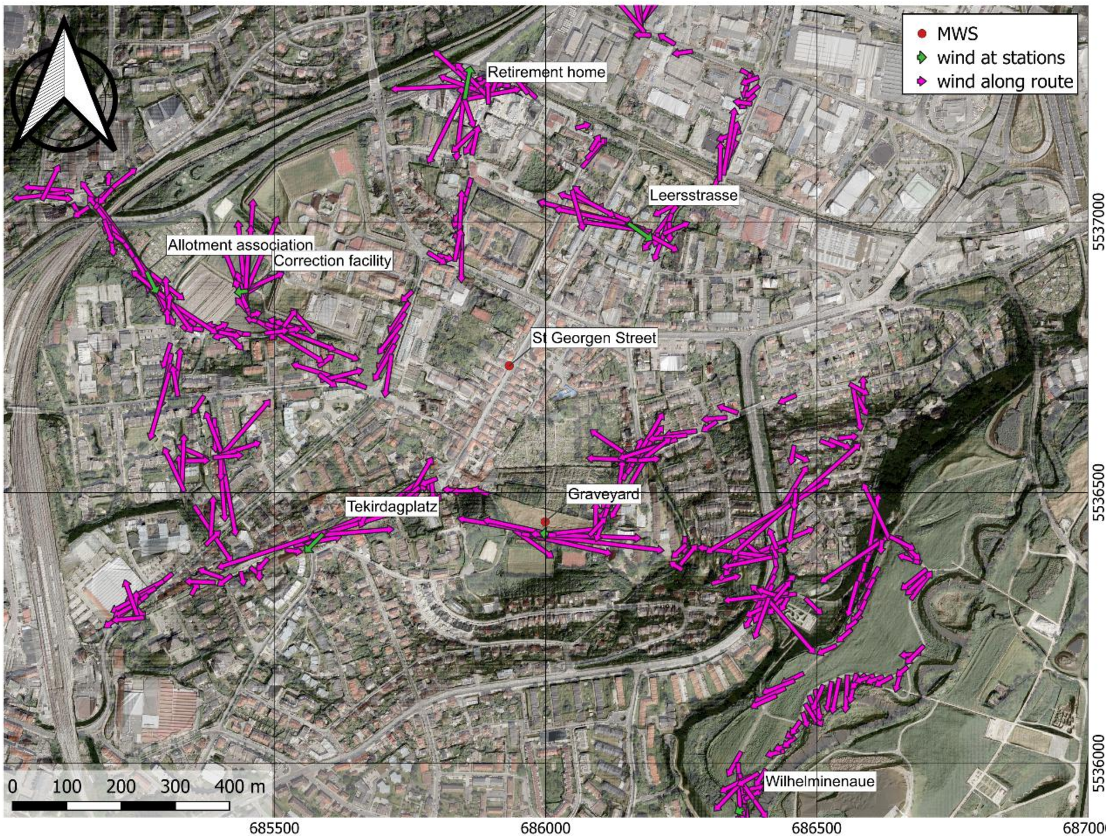

Figure A. 18 wind vectors of direction and speed along the measurement route on a map with relief shading (with z-factor 10) during the ride 00:00 – 00:59 CEST. Only data with windspeed > 0.5 ms-1 were used. The maximal windspeed during this ride was 5.47 m s^{-1}. The data were averaged over 4 second intervals, while for each station a mean over the complete stop was calculated. Along the route, the measurements are shown as blue arrows, and the station means are indicated with green arrows. Projection: ETRS89 / UTM zone 32N

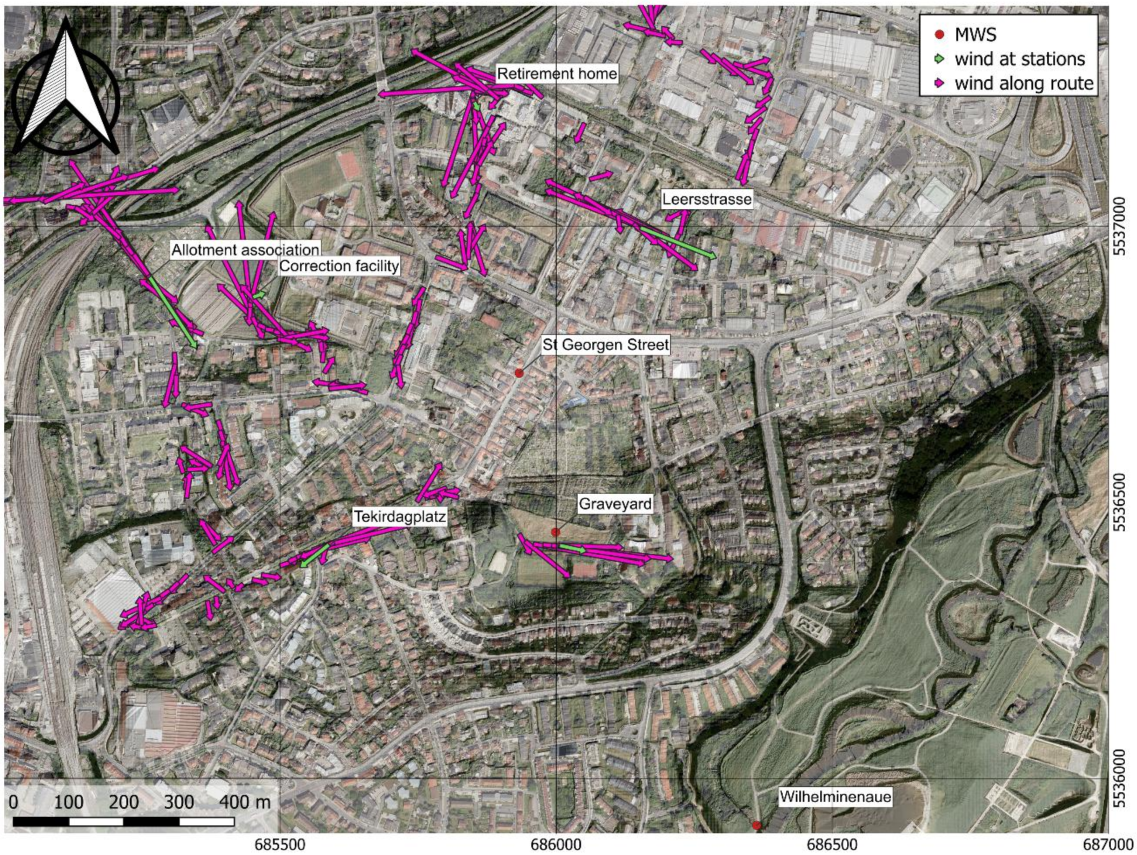

Figure A. 19 wind vectors of direction and speed along the measurement route on a map with relief shading (with z-factor 10) during the ride 04:24 – 04:59 CEST. Only data with windspeed > 0.5 ms-1 were used. The maximal windspeed during this ride was 5.43 m s^{-1}. The data were averaged over 4 second intervals, while for each station a mean over the complete stop was calculated. Along the route, the measurements are shown as blue arrows, and the station means are indicated with green arrows. Projection: ETRS89 / UTM zone 32N

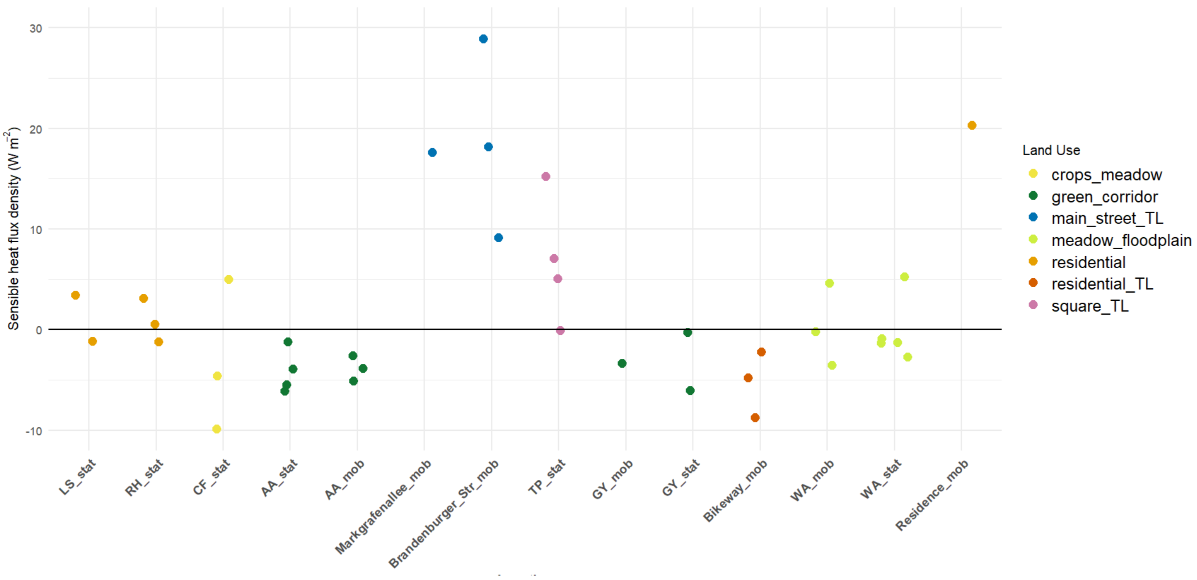

Figure A. 20 Sensible heat flux densities at the 00:00 CEST measurement ride. The x axis shows the different locations along the measurement route, marked with 'stat' for a stationary measurement, where the bike was parked, and with 'mob' for a mobile measurement, recorded while riding. The data points are colour coded according to the land use classifications shown in Figure 2.6.

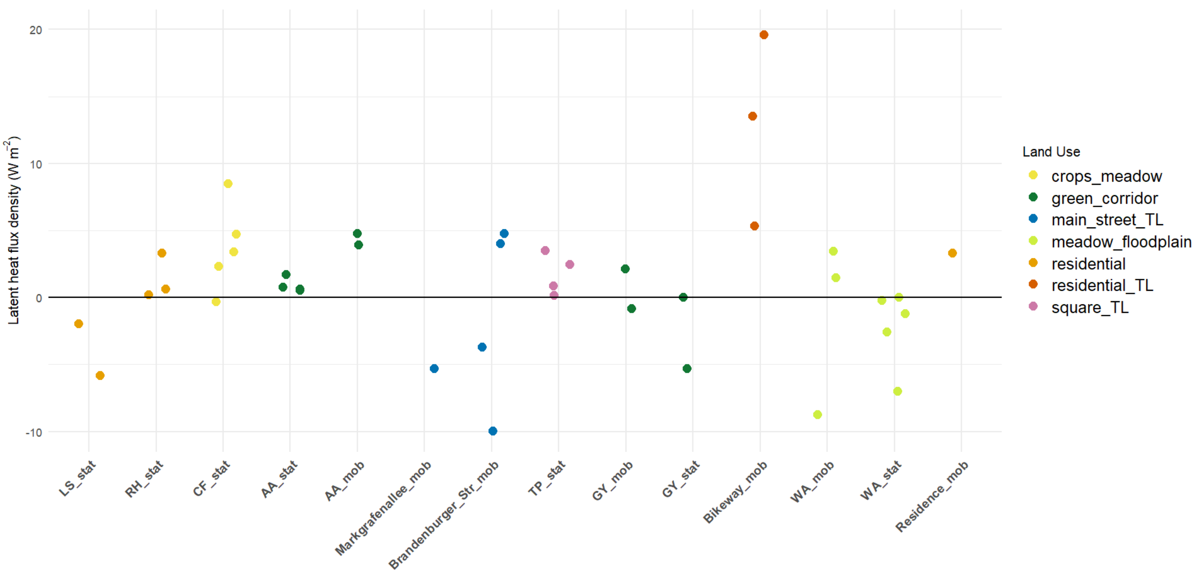

Figure A. 21 Latent heat flux densities at the 00:00 CEST measurement ride. The x-axis shows the different locations along the measurement route, marked with 'stat' for a stationary measurement, where the bike was parked, and with 'mob' for a mobile measurement during riding. The data points are colour coded according to the land use classifications shown in Figure 2.6.

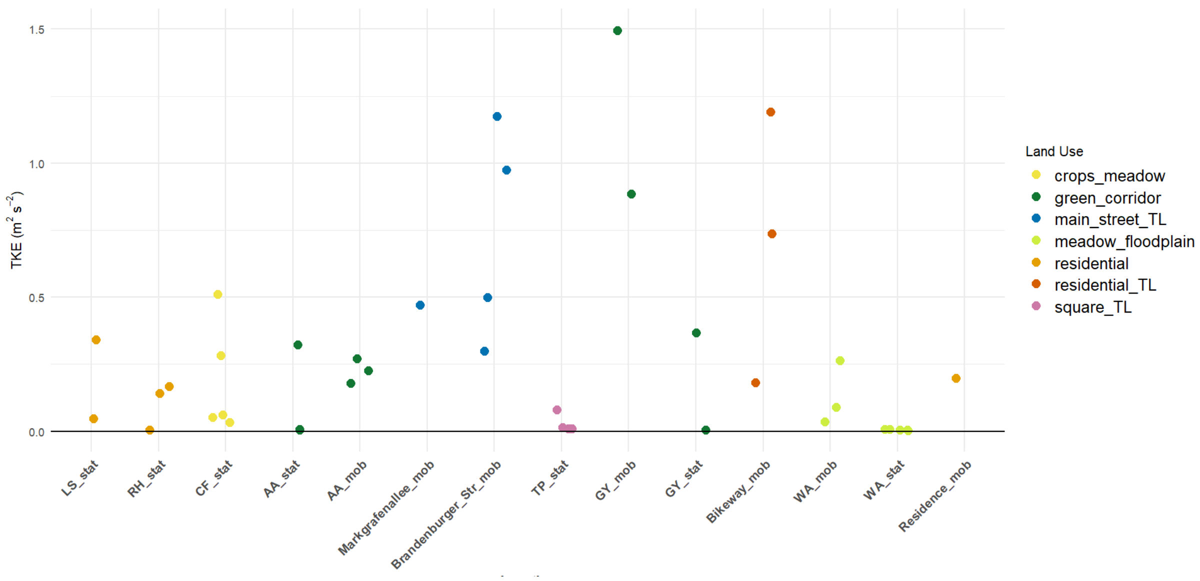

Figure A. 22 Turbulent kinetic energy at the 00:00 CEST measurement ride. The x-axis shows the different locations along the measurement route, marked with 'stat' for a stationary measurement, where the bike was parked, and with 'mob' for a mobile measurement, recorded while riding. The data points are colour coded according to the land use classifications shown in Figure 2.6.

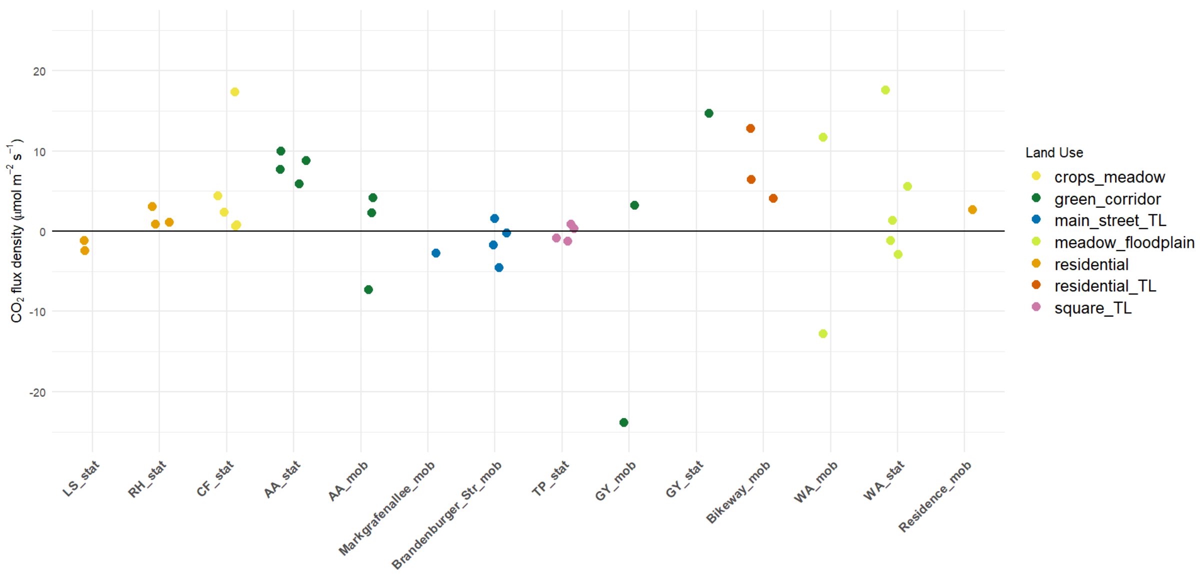

Figure A. 23 CO_2 flux densities at the 00:00 CEST measurement ride. The x-axis shows the different locations along the measurement route, marked with 'stat' for a stationary measurement, where the bike was parked, and with 'mob' for a mobile measurement, recorded while riding. The data points are colour coded according to the land use classifications shown in Figure 2.6.

Declaration of authorship

Hereby, I declare that I have authored the bachelor thesis titled "Characterizing summer nighttime urban heat island intensity and cold-air dynamics through mobile flux measurements and stationary sensor networks in a mid-sized city in central Europe" independently based on my own work. All direct or indirect sources used are acknowledged as references. This thesis has not been published or previously submitted to any other examination board.

Sophie Resch

Bayreuth, 22.09.2025

Location, Date Unterschrift